Texas A&M University

Mechanical Engineering Department

Turbomachinery Laboratory

Tribology Group

A CFD Model for Prediction of Leakage and Dynamic Force Coefficients in Pocket Damper Seals: from Gas to a Wet Gas

TRC-Seal-03-18

Research Progress Report to the Turbomachinery Research Consortium

by

Luis San Andrés
Mast-Childs Chair Professor
Principal Investigator

Jing Yang
Post-Doctoral Research Associate

Xueliang Lu
Research Assistant

May 2018

EXECUTIVE SUMMARY

Since their invention in 1991, pocket damper seals (PDS), elements that generate a large effective damping coefficient, find applications in high performance turbomachinery, in particular centrifugal compressors. Current and upcoming multiple-phase pump and compression systems in subsea (*ss*) production facilities must demonstrate long term operation and continuous availability. Sealing systems such as plain seals and labyrinth seals produce persistent subsynchronous rotor vibrations in these *ss* systems. Recently, however, a *wet* compressor incorporating a PDS operated stably where a labyrinth seal could not. The pockets apparently stopped the circulation of trapped liquid.

There is scant literature, experimental and numerical, addressing to PDSs handling a *wet* gas. This report, a first of its kind, presents experimental results and CFD predictions for leakage and force coefficients obtained for a fully partitioned pocket damper seal (FPPDS), four ribbed and with eight pockets/cavity, tested at the Turbomachinery Laboratory. The seal operates at a relatively low surface speed (35 m/s) and pressure drop (2.3 bar) while being supplied with a mixture of ISO VG 10 oi in air.

The research first built a CFD model for prediction of PDS performance and selected a (published) eight-ribs FPPDS supplied with air at 6.9 bar and exiting at ambient pressure. The rotor surface speed is 134 m/s. The CFD model, based on a mesh with a few millions nodes, produces pressure and velocity fields; and a three-dimensional flow model implementing a multi-frequency, elliptic orbit method delivers force coefficients. The CFD derived direct and cross coupled dynamic stiffnesses, H_R and h_R, agree well with the test data, whereas the direct damping C is slightly lower. The CFD details the contribution of each pocket to the seal force coefficients; the first row of pockets produces the largest centering stiffness and the lowest damping. Note that a bulk flow model is less accurate than the CFD model though it still captures most relevant trends.

As per the laboratory FPPDS; when supplied with just air (*dry*), the seal produces a direct stiffness (H_R) increasing with frequency and a relatively constant damping (C) and cross-coupled stiffness (h_R). The CFD predicted C agrees best with the test data albeit over predicting h_R at all frequencies and H_R at low frequencies. Under a *wet* gas condition with the liquid volume fraction (LVF) being just 0.4%, the experimental force coefficients show great variability vs. frequency, in particular the centering dynamic stiffness (H_R) that is negative, though growing with frequency on account of the large mass fraction, 57%. The CFD prediction inexplicably is opposite, $H_R > 0$.

Both *wet* gas experimental h_R and C are larger than their counterparts for the seal supplied with just gas. The CFD predictions (C, h_R) show a modest growth, *wet* vs. dry, yet they are lower than the test data. On the other hand, the CFD derived mass leakage for both components, air and oil, agrees perfectly with the measured ones.

Further work, experimental and CFD based, will continue to push the technology of *wet* gas seals while bridging the gap between test data and computational physics model simulations.

TABLE OF CONTENTS

LIST OF FIGURES

LIST OF TABLES

1. INTRODUCTION

Annular gas seals find wide application in compressors and turbines as they reduce secondary flows. The dynamic forced performance of annular gas seals may bring stability issues to a rotor-bearing system; hence seals with a high effective damping are favored in an industrial application.

In 1991, Vance and Shultz [1] invented a two-ribs, four-pocket damper seal (also called TAMSEAL®), by adding radial baffles (ridges) into the cavities of a conventional labyrinth seal (LABY). The pocket damper seal (PDS) has two unique characteristics, one is the ability to limit fluid rotation in the circumferential direction, and the other is its diverging clearance along the flow path. The novel PDS showed ~ 100 times more direct damping albeit 30% more leakage when compared to a conventional LABY of the same dimensions [2]. In 1999, Ransom et al. [3] present a test rig to systematically measure the rotordynamic force coefficients of a two-ribs LABY and a four-pocket PDS operating with a supply pressure ranging from 1 ~ 3 bar and rotor speed from 1,500 rpm to 3,000 rpm (ΩR = 10.0 m/s to 20.0 m/s). The LABY has a positive direct stiffness and a negative direct damping, whereas the PDS shows the opposite, i.e., a slightly negative direct stiffness and a positive direct damping. The leakage from both seals is similar.

In 2006, Ertas et al. [4] employ both the mechanical impedance method and the cavity dynamic pressure method to identify frequency dependent force coefficients of a twelve-ribs PDS and an eight-ribs PDS operating with a high supply pressure (up to 69 bar) and at a high rotor speed (up to 20,200 rpm, ΩR = 121 m/s). Besides the straight through PDSs, the test program also included PDSs (of the same dimensions) having downstream notches. These four PDSs show positive direct damping and same-sign cross-coupled stiffness, both of which are beneficial to the stability of a rotor-bearing system. The addition of downstream notches, forming a "convergent-divergent" flow resistance, drops the direct stiffness into a negative magnitude. In comparison with the force coefficients of the twelve-ribs PDS, a reduction in rib number (to eight-ribs) decreases the seal direct damping while increasing its direct stiffness.

The seals introduced above are known as a conventional type PDS. In 2002, Li et al. [5] test a new type of PDS, in which radial ridges separate all the plenums into pockets, i.e. all the cavities are active. Thus, the new type is named as a fully partitioned PDS (FPPDS). The test show the FPPDS, operating with a supply pressure up to 14.5 bar and rotor speed ranging up to 8,000 rpm (ΩR = 41 m/s), increases the rotor critical speed and lowers the motion amplification factor in comparison with those for a rotor mounted on a conventional PDS of the same dimensions. The

6

test results indicate the FPPDS has a positive direct stiffness and a higher direct damping in comparison with the coefficient of a conventional PDS. In 2007, Ertas and Vance [6] obtained experimental dynamic force coefficients of a FPPDS and a conventional PDS for operation at 69 bar supply space, rotor speed 20,200 rpm ($\Omega R = 121$ m/s), and under an excitation frequency range from 20 Hz to 300 Hz. The test results prove the FPPDS has a much higher positive direct damping coefficient and a larger direst stiffness than the conventional PDS under the same operating conditions. The test results are in accordance with early results in Ref. [5].

Later in 2012, Ertas et al. [7] investigate the rotordynamic performance of three types of annular gas seals; namely a honeycomb seal (HCS), a LABY, and a FPPDS, and obtain the seals rotordynamic force coefficients under a similar inlet circumferential pre-swirl velocity (0 or 60 m/s, swirl ratio $\alpha = 0.45$). The supply pressure is 6.9 bar and the rotor speed is 7 krpm or 15 krpm ($\Omega R = 62$ m/s or 134 m/s). The test data show the FPPDS and the HCS have a higher direct stiffness and direct damping than the coefficients from the LABY. The circumferential inlet pre-swirl and rotor speed have a great influence on the cross-coupled stiffnesses of the FPPDS and the HCS, while the cross-coupled stiffness of the LABY is only sensitive to the inlet pre-swirl. The experiments indicate the LABY is a good choice for an operating condition without inlet pre-swirl and a rotor spinning below the first mode critical speed. Otherwise, the FPPDS and the HCS have a superior dynamic forced performance.

As per predictive analyses, the Bulk flow model (BFM) has long been an efficient method to calculate the leakage and dynamic forced performance of annular seals. The first BFM for a PDS dates back to 1999 with Li et al. [8, 9] developing an isothermal, one-control-volume BFM. For a two-ribs, four-pocket PDS, the BFM predicted leakage matches well with their test data. Though the BFM under-predicts the direct stiffness and over-predicts the direct damping coefficient, the model still captures a negative direct stiffness and large direct damping coefficients. Li et al. [10], in follow up BFM predictions for a four-ribs, four-pocket PDS and comparisons against test data, also prove the model accuracy is acceptable for industrial applications.

Computational fluid dynamics (CFD) analysis of PDSs has recently come out of age. In 2012, for the eight-ribs PDS in Ref. [4], Li[1] et al. [11] successfully introduce a multi-frequency, elliptic whirl orbit model to solve the unsteady three-dimensional flow using a CFD analysis. The transient

---

[1] A different Li to the main author in Refs. [8-10].

response method implementing Fast Fourier Transform delivers the seal rotordynamic force coefficients. A good correlation of the CFD predicted force coefficients against test data by Ertas et al. [4] demonstrates the accuracy of the CFD method. A further CFD prediction by Li et al. [12] for an eight-ribs FPPDS also matches well with test data published by Ertas et al. in Ref. [7]. Li et al. [13] also investigate the influence of inlet/exit pressure ratio, rotor speed, and inlet pre-swirl on the leakage and rotordynamic force coefficient of a FPPDS first presented in Ref. [7]. Since the flow in an eight-ribs PDS is choked for operation at a supply pressure 6.9 bar and discharge at ambient pressure (1 bar), a variation in the exit pressure has a very small effect on the PDS rotordynamic coefficients. On the other hand, an increase in the supply pressure produces a significant increase of the seal direct stiffness and direct damping coefficients. With an increase in rotor speed, the direct damping and direct stiffness coefficients slightly increase. On the contrary, the effective damping coefficient reduces significantly. Including the pre-swirl circumferential velocity produces an increase in seal direct and cross-coupled stiffnesses and a decrease in effective damping. The results indicate a swirl brake does improve PDS stability. Li et al. [14] also discuss the effects of a partition wall type (conventional vs. fully partitioned), ridge number, and cavity depth on PDS forced performance. Compared with a conventional PDS, the FPPDS shows a larger direct stiffness and direct damping coefficients. Thus, the FPPDS has better stability characteristics than a conventional PDS, a finding in accordance with earlier test results by Ertas et al. [6]. The increase in the number of partition walls (pockets) increases the magnitude of the seal direct stiffness, cross-coupled stiffness and direct damping, as well as the effective damping when the excitation frequency is higher than the cross-over frequency[2]. The variation of the rotordynamic force coefficients for various cavity depths evidences there exists an optimum depth for a particular FPPDS. Thus, the CFD predictions do provide a useful guidance to better design FPPDS.

In 2016, Li et al. [15] evaluate and compare the rotordynamic coefficients obtained for a FPPDS and a LABY operating with either a high positive or a negative inlet pre-swirl. For the FPPDS, the inlet circumferential pre-swirl produces a weak effect on the seal direct stiffness and direct damping, whereas it has a dramatic effect on the cross-coupling stiffness and effective

---

[2] The whirl frequency at which the effective damping change signs, from negative to positive.

damping. As expected, applying a zero pre-swirl or negative pre-swirl (with a swirl brake) to the FPPDS enhances the seal stability.

Recently the PDS finds a promising application in liquid tolerant (*wet* gas) compression systems. Developments in centrifugal compressors call for *wet* gas operation as subsea factories must handle two-phase flows with a liquid volume fraction (LVF) as high as 5%. Note that the issue of a liquid trapped induced rotordynamic instability challenges *wet* gas compressor operation. In 2014, Vannini et al. [16] report a severe sub synchronous rotor vibration (SSV) at 0.45X in a single stage centrifugal compressor in which a LABY operated with a 3% LVF wet gas. Replacing the LABY with a FPPDS successfully eliminated the rotor SSV [17]. Further experimental and CFD analyses demonstrate the ridges in a PDS reduce and decelerate the liquid trapped in the cavities, and which aids to increase seal stability. Thus, PDSs have a demonstrated performance in *wet* gas compression systems. However, few CFD analyses for a *wet* gas PDS are published, in particular concerning rotordynamic force coefficients. Note that Vannini et al. [17], relying on CFD predictions, explain the favorable behavior of their *wet* gas PDS, alas without assessing its dynamic force coefficients.

In this report, a three-dimensional CFD analysis predicts the leakage and rotordynamic force coefficients of an eight-ribs, eight-pocket FPPDS ($L/D = 0.6$, $C_r = 0.3$ mm) introduced in Ref. [7], operating under a supply pressure $P_s = 6.9$ bar and rotor speed 15,000 rpm ($\Omega R = 133.5$ m/s). The procedure uses a multi-frequency elliptic orbit method with the Discrete Fourier Transform (DFT) to derive the seal dynamic force coefficients. The good match of the CFD predictions against the test data provides confidence for further numerical analyses.

As detailed above, the Turbo Lab at TAMU has a long research history on PDSs since their inception. A test rig in the Laboratory has produced comprehensive data for the leakage and dynamic force coefficients of *wet* gas annular seals supplied with a mixture of air in ISO VG10 oil, including a smooth surface annular seal [18-19], a three-wave annular seal [20], a grooved seal, and an upstream step clearance seal and a downstream step clearance seal [21]. As a complement of the research, a four-ribs, eight-pocket FPPDS ($L/D = 0.38$, $C_r = 0.184$ mm) is under going tests to measure its leakage and force coefficients under a *wet* gas condition operation.

In an earlier numerical investigation for a smooth surface annular seal operating with a *wet* gas [22], the CFD predictions match well the test data in Ref. [19] for a low pressure drop and laminar flow condition. CFD predictions can provide flow details like the mixture axial velocity, swirl ratio

and LVF variation. Hence, it is meaningful to perform CFD analysis of the four-ribs, eight-pocket FPPDS. Therefore, this report includes both measured and CFD predicted leakage and dynamic force coefficients for the test FPPDS operating with both pure air and an air and oil mixture. The results help to understand how a FPPDS works under either a pure gas or a *wet* gas condition.

2. CFD ANALYSIS OF A FULLY PARTITIONED POCKET DAMPER SEAL

The following details an investigation to obtain the rotordynamic force coefficients of an eight-ribs fully partitioned pocket damper seal (FPPDS) [7] with geometry and operating conditions listed in Table 1. Figure 1 displays a sketch of a cross-section of the FPPDS with geometry information for better understanding. There are seven sections along the axial length of the seal, each with eight pockets, their length is either 13.97 mm or 6.35 mm. 3.175 mm in length ribs, making a thin film land with clearance $C_r = 0.3$ mm, separate one pocket from another one, each 3.175 mm depth. There are eight *ridges* or partition walls along the circumferential direction, thus the number of pocket equals eight.

Table 1 Geometry and operating conditions of an eight-ribs fully partitioned pocket damper seal. Taken from Ref. [7].

Seal length, L	102.87 mm
Rotor diameter, D_r	170 mm
Stator diameter, D_s	170.6 mm
Clearance height, C_r	0.3 mm
Number of ribs	8 (axial)
Number of partition walls (ridges)	8 (circumferential)
Pocket length, L_C	13.97 mm / 6.35 mm
Pocket depth, d	3.175 mm
Rib axial thickness, δ	3.175 mm
Working fluid	Air (ideal gas)
Supply pressure, P_S	6.9 bar (a)
Exit pressure, P_a	1 bar (a)
Supply temperature, T_S	287.15 K
Density of fluid at (P_S, T_S), ρ_S	8.38 kg/m^3
Kinematic viscosity at (P_S, T_S), ν_S	2.13×10^{-6} m^2/s
Rotor speed, Ω	15,000 rpm
Surface speed, ΩR	133.5 m/s
Sound speed $a = \sqrt{\gamma RT}$ at T_S	340 m/s
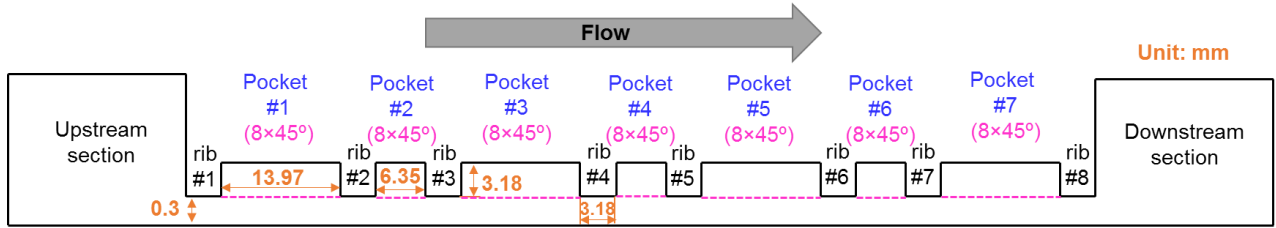
Fig. 1 Cross-section view of an eight-ribs pocket damper seal (not to scale).

Figure 2 displays the mesh for the seal with additional upstream and downstream sections. The mesh node is about 7.3×10^6. Table 2 lists the details of the mesh node number for the FPPDS. In order to prove the reliability of the mesh, a grid independence analysis employs a finer mesh (node account 10×10^6). A comparison of CFD predictions obtained for the two set of meshes demonstrates the mesh with 7.3×10^6 node is fine enough.
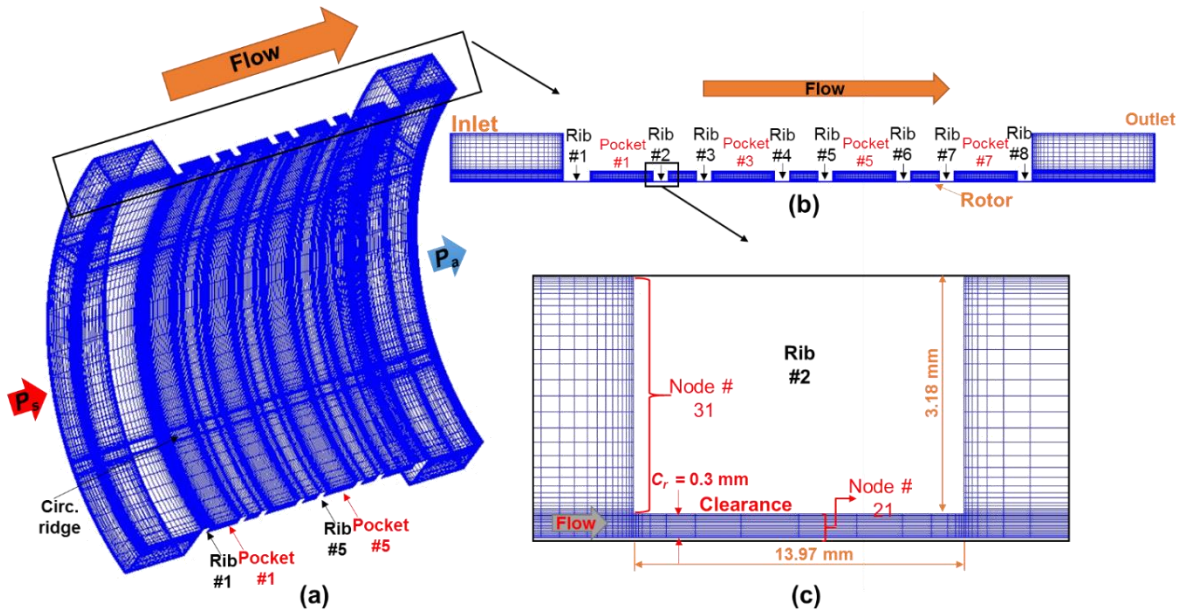
Fig. 2 Three-dimensional mesh for a pocket damper seal. (a) ¼ cut (90º) of 3D mesh; (b) a cross section view of the mesh; (c) mesh details on second rib.

Table 2 Mesh node distribution of an eight-ribs fully partitioned pocket damper seal in Ref. [7].

Radial node # in clearance	21
Radial node # in pocket	31
Axial node # for a rib	19
Axial node # in pocket	57 / 25
Circumferential node #	336 (for 360º)

11

A commercial CFD software (ANSYS Fluent®) solves the Reynolds-Averaged Navier-Stokes (RANS) equations. The turbulence flow model is a realizable k-ε model with a scalable wall function. The air is an ideal gas supplied at temperature $T_S = 287$ K. The pressures at the seal inlet (upstream section) and outlet are set as $P_S = 6.9$ bar (a) and $P_a = 1$ bar (a), respectively. The circumferential speed of the fluid is set as zero at the inlet of the upstream section, except at the bottom wall that represents the spinning rotor with surface speed (ΩR). The non-slip fluid velocity condition applies to both rotor and stator surfaces.

In a steady-state CFD model, the rotor spins at 15,000 rpm ($\Omega R = 134$ m/s). The gas upstream of the seal has no swirl. The CFD predicted mass leakage is 108.6 g/s, ~ 2% lower than the CFD prediction (110.4 g/s) by Li et al. [13]. The leakage predicted by using the finer mesh (node count 1×10^7) is 108.5 g/s, which agrees with the prediction of the medium mesh. Note the authors in [7] do not report the measured leakage. A bulk-flow model (PD_Seal®) [10] predicts a leakage equal to 104.4 g/s under the same operating conditions.

Figure 3 shows a circumferential mid-plane through cavities and a mid-plane under ridges. The circumferential mid-plane under the ridges is a plane with uniform film width, $C_r = 0.3$ mm. On these two mid-planes, Figure 4 displays the CFD predicted average static pressure along the flow direction. The solid black squares stand for the BFM predicted average pressure in the pockets. The decrease of static pressure happens mainly at the locations where the fluid leaves a pocket. For the flow under the ridges, the static pressure reduces earlier, before the location where the fluid leaves a cavity. The pressure drop (ΔP) is large in the last rib (#8). Note the BFM predicted static pressures are a tiny lower than the CFD results.
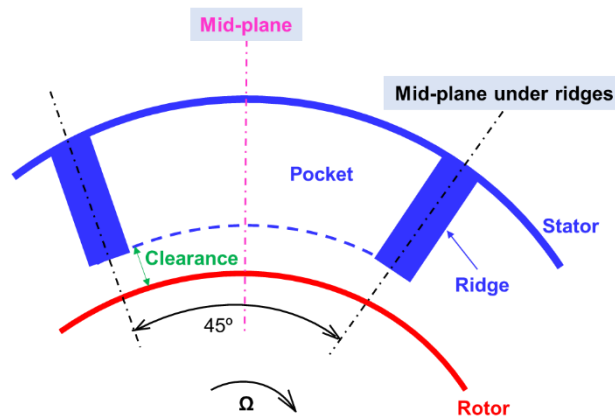
Fig. 3 Cross-section view of a pocket and ridges with section at mid-plane for displaying CFD results (not to scale)**.**
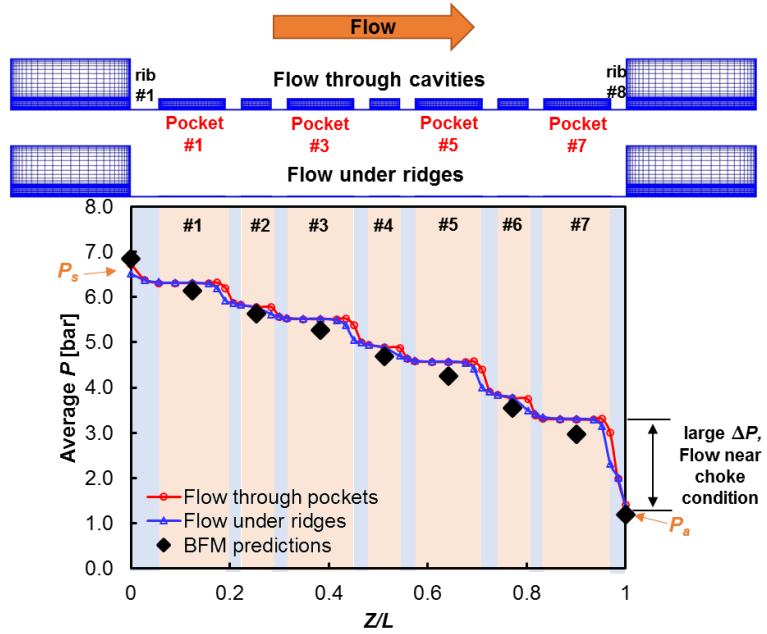
Fig. 4 CFD predicted average static pressure at the mid-plane of a pocket and under adjacent ridges vs. axial direction; BFM predicted static pressure also shown. Fully partitioned PDS, $L/D = 0.6$, $C_r = 0.3$ mm, $P_s = 6.9$ bar, rotor speed 15,000 rpm ($\Omega R = 134$ m/s).

Figure 5 displays the CFD predicted cross-film average axial velocity W and swirl ratio α along the flow direction. The swirl ratio (α) equals the cross-film average circumferential velocity divided by the rotor surface speed, i.e. $\alpha = U_\theta/(\Omega R)$. When the fluid passes under a rib, the average axial velocity is almost constant, while the swirl ratio keeps increasing. When the fluid enters a pocket, both the axial velocity and circumferential velocity decrease because of the increase in cross section area. At the final rib (#8), the fluid accelerates to ~320 m/s while the sound speed a = 340 m/s at a supply temperature T_S = 287 K. The Mach number Ma = (W/a) ~ 0.94. Thus, the flow is almost choked at the exit plane. Note the circumferential swirl velocity ratio is still low at the exit of the PDS, α ~ 0.22.
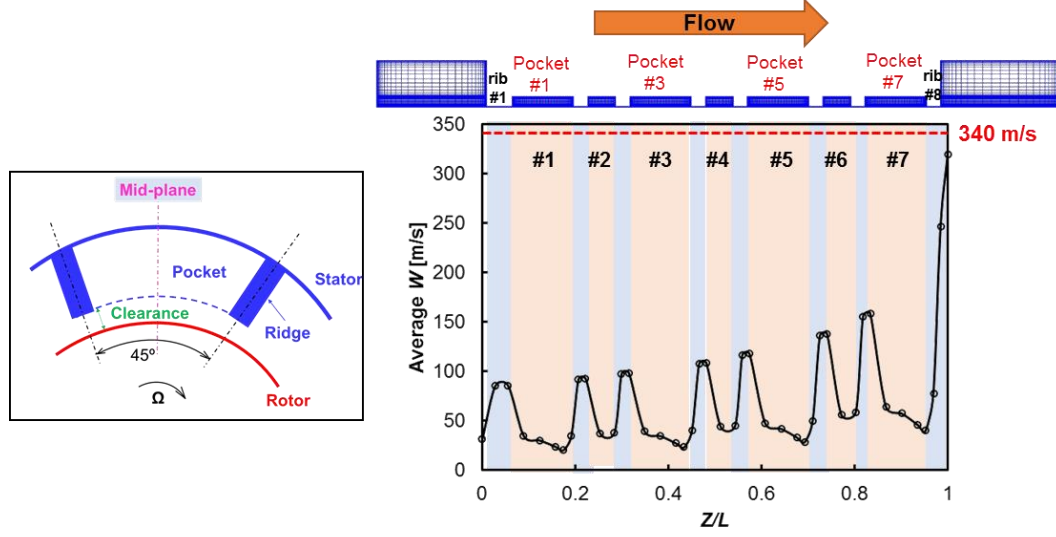
(a) Average axial velocity W [m/s]
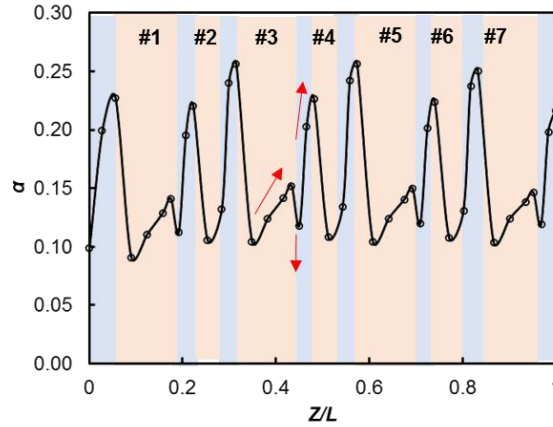
(b) Swirl ratio

Fig. 5 CFD predicted average axial velocity W and circumferential swirl ratio (α) at the mid-plane of a pocket. Fully partitioned PDS, L/D = 0.6, C_r = 0.3 mm, P_s = 6.9 bar, rotor speed 15,000 rpm (ΩR = 134 m/s).

Derivation of rotordynamic force coefficients

A three dimensional unsteady flow CFD predicts the rotordynamic force coefficients of the FPPDS under the operating condition listed in Table 1. The multi-frequency orbit method by Li et al. [11] is applied to extract the rotordynamic force coefficients over a range of discrete excitation frequencies. The procedure obtains a quasi-periodic flow solution for rotor displacements comprising a superposition of excitation frequencies. The dynamic displacements of the rotor center are,

$$d_{x(t)} = a\sum_{i=1}^{N} \cos(\omega_i t); \ d_{y(t)} = b\sum_{i=1}^{N} \sin(\omega_i t) \tag{1}$$

14

where $a = 0.1 C_r/N$, $b = \frac{1}{2} a$, and $\{\omega_i\} = 20$ Hz, 40 Hz, ...260 Hz ($N = 13$). The time elapsed for a complete period of multiple-frequency excitation $T = 0.05$s, as determined from the smallest excitation frequency (20 Hz). The time step is 0.1 ms (500 steps to complete T=50 ms). After the numerical flow has converged, a Discrete Fourier Transform (DFT) of the time varying forces, over time span T= 0.05s, produces the component of forces in the frequency domain. Note the DFT frequency resolution $\Delta f = 1/T = 20$ Hz.

For a centered annular seal[3], the reaction forces $\mathbf{F} = [f_x, f_y]^T$ related to the rotor displacements $\mathbf{D} = [d_x, d_y]^T$ are,

$$-\begin{bmatrix} f_x \\ f_y \end{bmatrix} = \begin{bmatrix} \bar{H} & \bar{h} \\ -\bar{h} & \bar{H} \end{bmatrix} \begin{bmatrix} d_x \\ d_y \end{bmatrix} \tag{2}$$

where $\bar{H}$ and $\bar{h}$ are the direct and cross-coupled impedances, respectively.

In the frequency domain, Eq. (2) become,

$$-\begin{bmatrix} F_{X(\omega_j)} \\ F_{Y(\omega_j)} \end{bmatrix} = \begin{bmatrix} H_{(\omega_j)} & h_{(\omega_j)} \\ -h_{(\omega_j)} & H_{(\omega_j)} \end{bmatrix} \begin{bmatrix} D_{X(\omega_j)} \\ D_{Y(\omega_j)} \end{bmatrix}, j = 1, \dots, N \tag{3}$$

where $H_{(\omega_j)}$ and $h_{(\omega_j)}$ are the complex direct and quadrature dynamic stiffnesses. $D_{X(\omega_j)} \to a$, $D_{Y(\omega_j)} \to -i\, b$ are the complex rotor center displacements at frequency ω_j and i is the imaginary unit. From Eq. (3), the complex direct and quadrature dynamic stiffnesses are,

$$H_{(\omega_j)} \leftarrow -\frac{\left(aF_{X(\omega_j)} - ib\, F_{Y(\omega_j)} \right)_j}{\left(a^2 - b^2 \right)}; \; h_{(\omega_j)} \leftarrow \frac{\left(aF_{Y(\omega_j)} + i\, bF_{X(\omega_j)} \right)}{\left(a^2 - b^2 \right)}, j = 1, \dots, N \tag{4}$$

Let

$$H_{(\omega_j)} = H_R + iH_I; h_{(\omega_j)} = h_R + ih_I \tag{5}$$

where H_R and h_R denote the direct and cross-coupled dynamic stiffnesses, both functions of frequency. Subscripts R and I stand for the real (R) and imaginary (I) parts of the force coefficients.

The representation $H_R = (K - \omega^2 M)$, $h_R = (k - \omega^2 m)$, and $H_I \sim (C\omega)$ is strictly valid for a seal lubricated with an incompressible fluid only, and for which K an k represent the seal direct and

---

[3] Note: only one excitation is needed to fully characterize the force coefficients. This brings 50% saving in computation time!

cross-coupled stiffness, M is the inertia term, and C stands for the direct damping coefficient, $C \sim$ (H_I/ω).

CFD predictions of rotordynamic force coefficients and comparisons to test data

One three-dimensional unsteady state case employs 40 cores in a computer cluster provided by the High Performance Research Center (HPRC) at TAMU. It takes ~50 h CPU time to compute one period (500 steps per period) of rotor whirl motion. The computations takes at least four periods (4T) to converge, i.e., as defined by a difference of less than 3% for the CFD predicted force coefficients (H_R, h_R, and C) from the third period and fourth period.

Figure 6 displays the direct dynamic stiffness (H_R), cross-coupled dynamic stiffness (h_R), direct damping ($C \sim H_I/\omega$), and effective damping coefficient (C_{eff}) vs. frequency (ω/Ω), including the present CFD predictions, the test data in Ref. [7], and the BFM predictions derived from *PD_Seal*®. The effective damping coefficient shown in Figure 6(d) is

$$C_{eff} = \frac{H_I - h_R}{\omega_j} , j = 1, \ldots, N \tag{6}$$

Figure 6 includes both CFD predictions obtained with the medium mesh (node count 7.3×10^6) and a finer mesh (node count 1×10^7). The force coefficients obtained by the two meshes match each other. The good agreement proves the mesh with node count 7.3×10^6 is fine enough.

The CFD predicted dynamic direct stiffness (H_R) is a little higher than the test data, whereas the BFM predictions are lower than the experimental results, negative for $\omega < 200$ Hz. The CFD prediction of the cross-coupled dynamic stiffness (h_R) is close to the test data. Both the CFD and BFM predicted direct damping coefficients decrease with an increase in ω, though the predictions are lower than the test data.

The effective damping (C_{eff}) delivered by CFD is ~40% lower than the test data. Note the BFM predicted C_{eff} is negative at all excitation frequencies. It is easy to estimate the cross-over frequency when $C_{eff} > 0$. The CFD predicted magnitude is ~ 66 Hz, higher than the experimentally derived result (~ 40 Hz).
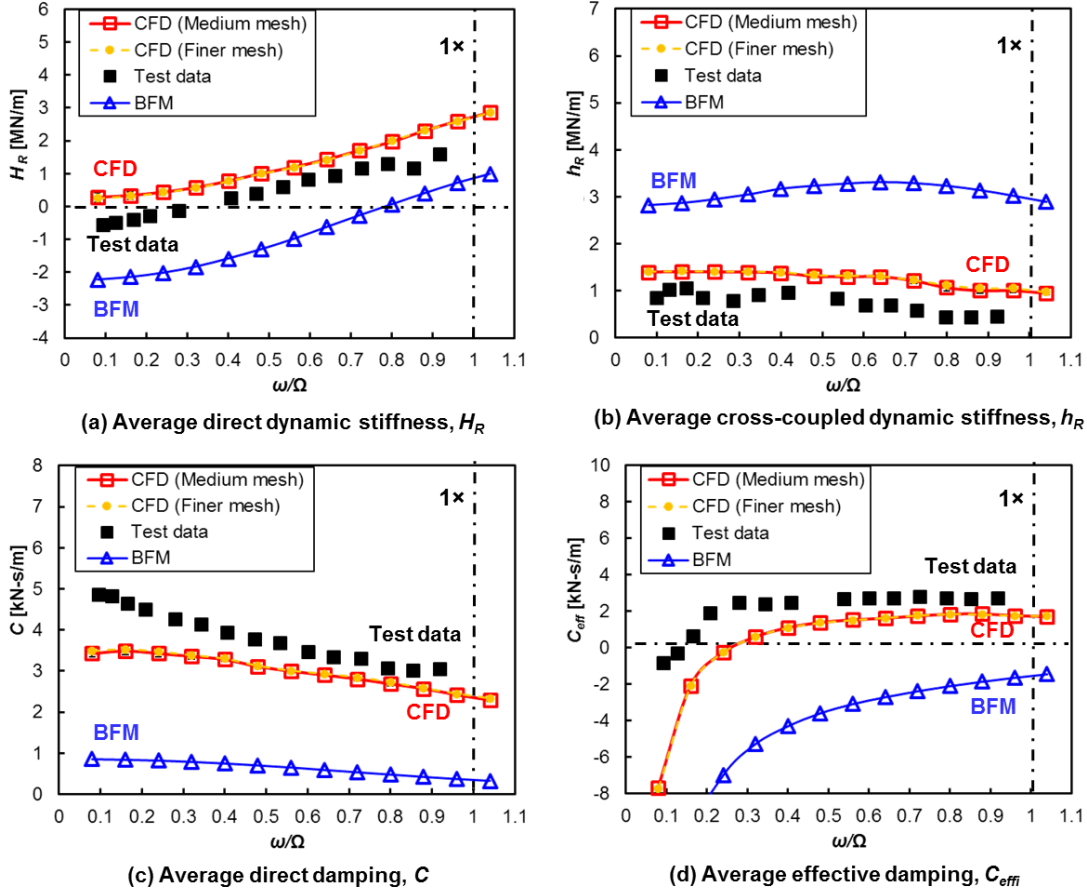
Fig. 6 CFD and BFM predicted, and test force coefficients for a pocket damper seal vs. frequency ratio (ω/Ω). (a) Direct dynamic stiffness H_R, (b) Cross-coupled dynamic stiffness h_R, (c) Direct damping C, (d) Effective damping C_{eff}. Test data from Ref. [7]. Fully partitioned PDS, L/D = 0.6, C_r = 0.3 mm, P_s = 6.9 bar, rotor speed 15,000 rpm (ΩR = 134 m/s).

CFD predicted rotordynamic force coefficients on each pocket

Further analysis helps to understand the influence of each pocket to the generation of the rotordynamic force coefficients. Figure 7 displays the CFD predicted direct dynamic stiffness H_R, cross-coupled dynamic stiffness h_R, and direct damping C divided by pocket length on each of the seven pockets. The coefficients for the even # pockets (# 2, 4, and 6) share similar trends with those for the odd # pockets (# 1, 3, 5, and 7).

Note (H_R/L_C) in all pockets increases with excitation frequency ω. Among all the seven pockets, the #2 pocket brings the largest positive stiffness (H_R/L_C). On the other hand, the #7 pocket has the most negative H_R/L_C (when ω/Ω < 0.72). The even # pockets show similar magnitude for h_R/L_C as the coefficients for the odd# pockets, and the # 1 pocket has the smallest h_R/L_C than the rest. The direct damping coefficients (C/L_C) for each pocket decrease slightly with an increase in

ω. The #5 and #7 pockets have the highest damping than the other pockets, whereas the #1 pocket shows the least damping. The numerical predictions are useful to better realize the design and performance optimization of a FPPDS.

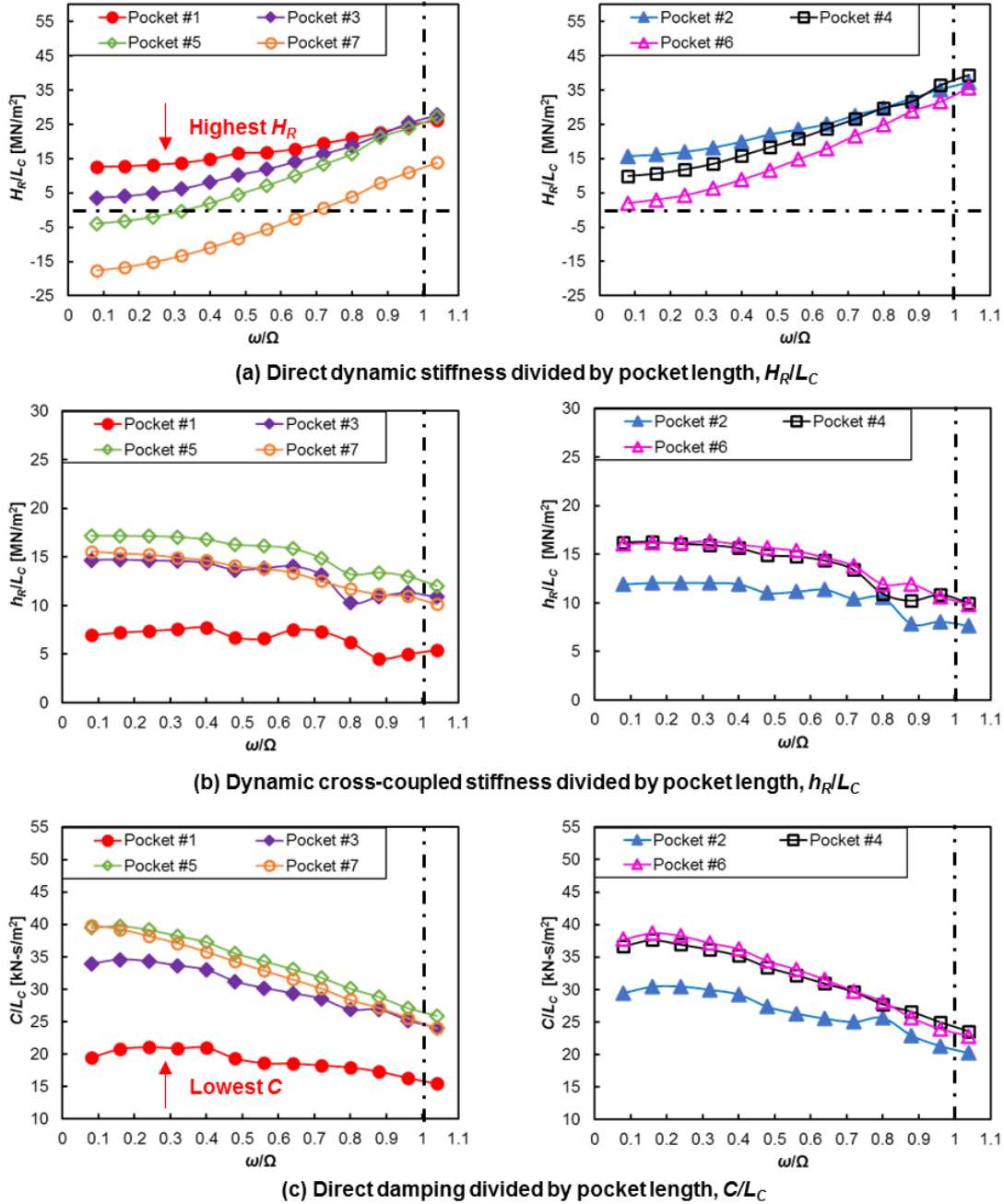**Fig. 7 CFD predicted rotordynamic force coefficients for each pocket divided by its length vs. frequency ratio (ω/Ω). (a) Direct dynamic stiffness (H_R/L_C), (b) Cross-coupled dynamic stiffness (h_R/L_C), (c) Direct damping (C/L_C).** Fully partitioned PDS, $L/D = 0.6$, $C_r = 0.3$ mm, $P_s = 6.9$ bar, rotor speed 15,000 rpm ($\Omega R = 134$ m/s).

Closure

The section showed the numerical (CFD and BFM) predictions for an eight-ribs FPPDS (L/D = 0.6, C_r = 0.3 mm) against test data in Ref. [7]. The FPPDS operates with supply pressure P_S = 6.9 bar and rotor speed 15,000rpm (ΩR = 134 m/s). The CFD predictions show how the cross-film average static pressure P, axial velocity W, and circumferential swirl ratio α vary along the flow direction. A three-dimensional unsteady flow CFD implementing a multi-frequency, elliptic orbit method delivers the rotordynamic force coefficients vs. frequency (ω). The CFD predicted direct dynamic stiffness H_R and cross-coupled dynamic stiffness h_R match well the test data. The direct damping C is slightly lower than the measured one. The comparisons give confidence on the CFD procedure. Though the BFM under estimates H_R and C and over predicts h_R, the BFM predictions still capture the variation trends for the rotordynamic coefficients. CFD allows to predict the influence of each pocket on the generation of rotordynamic force coefficients. All pockets share similar trends. Note that the #1 pocket (near inlet) produces the largest positive direct stiffness H_R and smallest damping C coefficients.

3. CFD ANALYSIS OF A FULLY PARTITIONED POCKED DAMPER SEAL TESTED AT THE TURBO LAB

Currently there is a fully partitioned pocket damper seal (FPPDS) under testing at the Turbomachinery Laboratory. Figure 8 displays a half view (180º cut) of the FPPDS having four ribs along the axial seal length and eight ridges or partition walls in the circumferential direction. Thus, the number of pockets equals eight. Figure 9 shows a cross-section plane of the FPPDS with dimensions and Table 3 lists the PDS geometry information and operating conditions.

San Andrés and Lu [18-19] detail the test procedure to procure dynamic force coefficients from a *wet* seal test rig. At a shaft speed of 5,250 rpm (ΩR=35 m/s), a *wet* gas (ISO VG10 oil in air) flows into the pocket damper seal at a fixed supply pressure (P_S). Two electromagnetic shakers with a load capacity of 440 N each, deliver unidirectional periodic loads (with a frequency 10-120 Hz) to the seal housing, flexibly supported. Two load cells installed on the seal housing record the applied loads, two eddy current sensors and two piezoelectric accelerometers record the ensuing seal housing motions and accelerations. Based on the measured loads, displacements, and accelerations, a physical model delivers the dynamic force coefficients. For more details of the test rig, see Refs. [18-19].

This section details the CFD predictions of leakage and rotordynamic force coefficients for the PDS against test data measured for operation at a low supply pressure and ambient exit pressure.
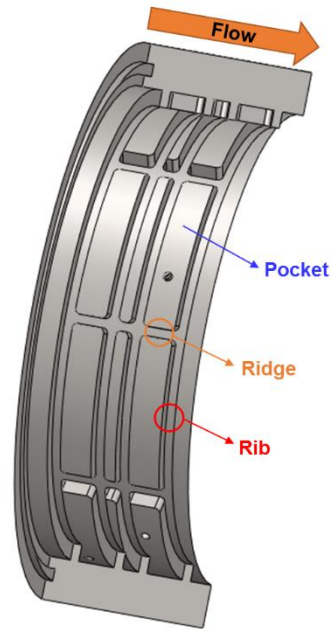
Fig. 8 View of a four-ribs, fully partitioned pocket damper seal (180⁰ cut).
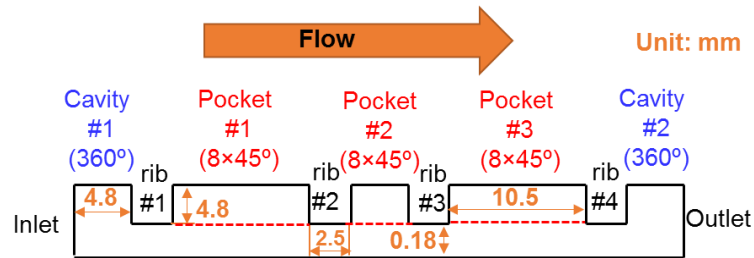
Fig. 9 Cross-section of a four-ribs, fully partitioned pocket damper seal (not to scale).

Table 3 Geometry and operating conditions of a four-ribs fully partitioned gas pocket damper seal.

Seal length, L	48 mm
Rotor diameter, D_r	127 mm
Stator diameter, D_s	68.484 mm
Clearance height, C_r	0.184 mm
Number of *ribs*	4 (axial)
Number of partition walls (ridges)	8 (circumferential, 45°)
Pocket length, L_C	10.5 mm / 4.8 mm
Pocket depth, d	4.8 mm
Rib axial thickness, δ_{rib}	2.5 mm

Working fluid	Air (ideal gas)
Supply pressure, P_S	1.6, 2.3, 3.2 bar (a)
Exit pressure, P_a	1 bar (a)
Supply temperature, T_S	315 K
Density of gas at (P_S, T_S), ρ_S	1.14 kg/m^3
Kinematic viscosity at (P_S, T_S), μ_S	1.8×10^{-5} kg/(m·s)
Rotor speed, Ω	5,250 rpm
Surface speed, ΩR	35 m/s
Sound speed $a = \sqrt{\gamma RT}$ at T_S	356 m/s

Figure 10 displays the mesh for the FPPDS. The mesh node is about 3.6×10^6. Since there is a shallow cavity (360º) before the first (#1) rib and another after the last (#4) rib, there is no need to add extra upstream or downstream sections in the CFD analysis. The radial mesh node distribution within the seal clearance is uniform, the node # is 21. Table 4 lists the details of the mesh node number. A finer mesh with node count 5.7×10^6 is employed in the grid independence analysis. The comparison of CFD predictions by these two meshes shown later demonstrates the fidelity of the mesh with node count 3.6×10^6.
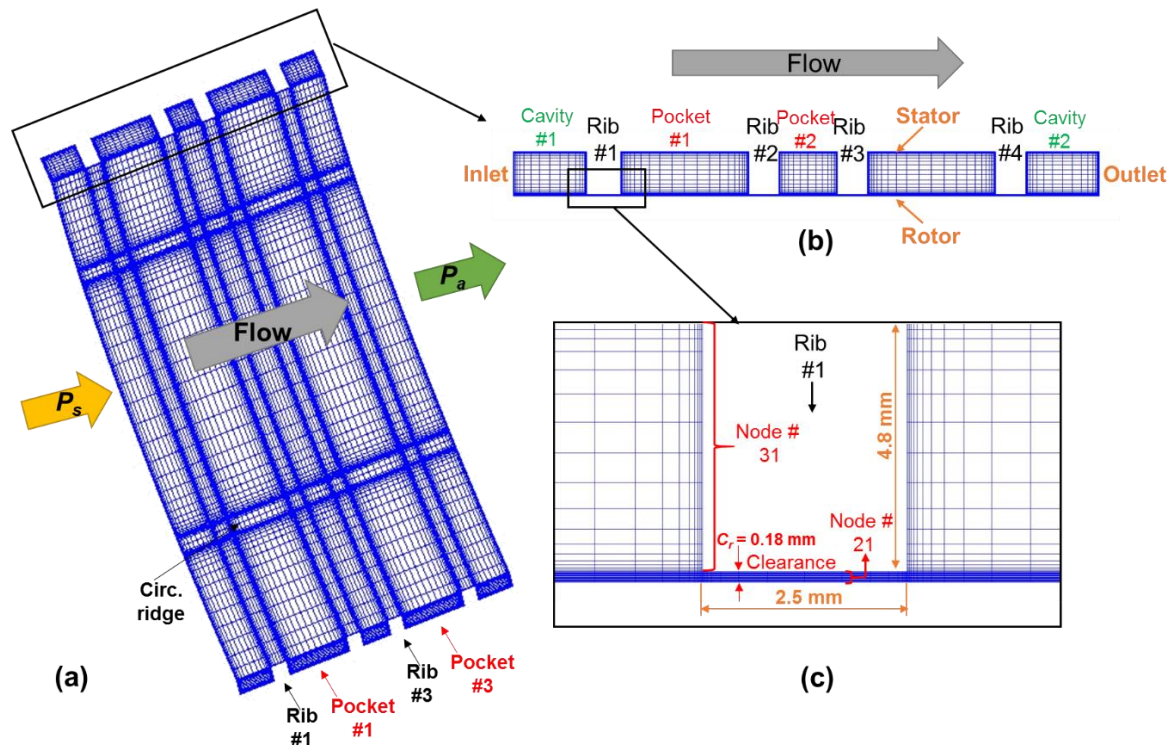
Fig. 10 Three-dimensional mesh for a four-ribs fully partitioned pocket damper seal. (a) ¼ cut (90⁰) of the three-dimensional mesh; (b) a cross section of the mesh; (c) mesh details for first rib.

Table 4 Mesh node distribution of a four-ribs fully partitioned pocket damper seal.

Radial node # in clearance	21
Radial node # in pocket	31
Axial node # for a rib	15
Axial node # in pocket	45 / 31
Circumferential node #	368

The analysis employs a commercial CFD software (ANSYS Fluent®). All the numerical setups are identical to those detailed in the last section and not repeated here. The pressure at the seal inlet plane is set as P_S = 1.6, 2.3 or 3.2 bar (a), the pressure is ambient, P_a = 1 bar (a), at the exit plane, the rotor spins at 5,250 rpm (ΩR = 35 m/s), and the inlet pre-swirl ratio α = 0.

A three-dimensional steady state CFD analysis predicts the FPPDS leakage against the test data. A BFM (*PD_Seal*®) also produces predictions under the same operating condition listed in Table 3. Figure 11 depicts the CFD, BFM predicted and measured leakage vs. pressure ratio (P_S/P_a). The CFD predicted leakage matches well with the test data, in particular for P_S/P_a >1.5. The prediction by the BFM is lower than the measured leakage, ~ 8% at pressure ratio (P_S/P_a) = 2.

The CFD predictions of the PDS leakage vs. (P_S/P_a) obtained by using a finer mesh (node count 5.7×10^6) are all within 1% of those obtained with the medium mesh (node count 3.6×10^6). These predictions are not shown for brevity.
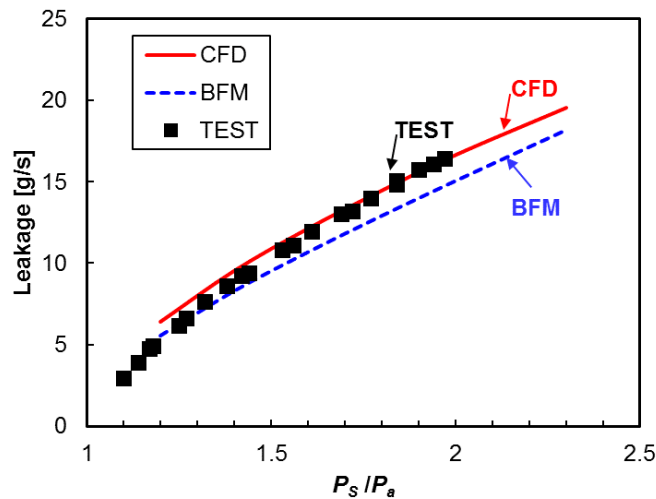
Fig. 11 CFD and BFM predicted and measured leakage vs. pressure ratio (P_S/P_a). Fully partitioned PDS, L/D = 0.38, C_r = 0.184 mm, rotor speed 5,250 rpm (ΩR = 35 m/s).

Figure 12 depicts the CFD and BFM predicted cross-film average pressure ratio (P/P_a) at a mid-plane of a pocket (see inset) for operation with P_S = 1.64 bar (a), 2.3 bar (a), and 3.2 bar (a). For the CFD prediction, P is almost constant within a pocket. The static pressure decreases when the gas leaves a pocket and flows below a rib. The BFM predicted P is lower than the CFD results, in particular at the highest supply pressure P_S = 3.2 bar (a). Figure 13 displays the cross-film average axial velocity (W) and circumferential velocity swirl ratio (α) along the flow direction. Recall at the seal inlet, the axial velocity is ~ 3.5 m/s and the circumferential velocity is zero. The fluid accelerates when leaving a pocket into a film below a rib. The axial velocity increases gradually passing under each rib. For a supply pressure P_s = 3.2 bar (a), the fluid average axial velocity below the #4 rib increases from 215 m/s towards 292 m/s, and the Mach number (Ma = W/a) increases to ~ 0.8. In the first cavity (#1), the swirl ratio (α) is very low and increases slightly to 0.02. The swirl ratio α further increases when the gas enters a film below a rib and decreases when the gas enters a pocket. Note α <0.3 for all P_S, as the FPPDS is short in length (L/D_r = 0.38).
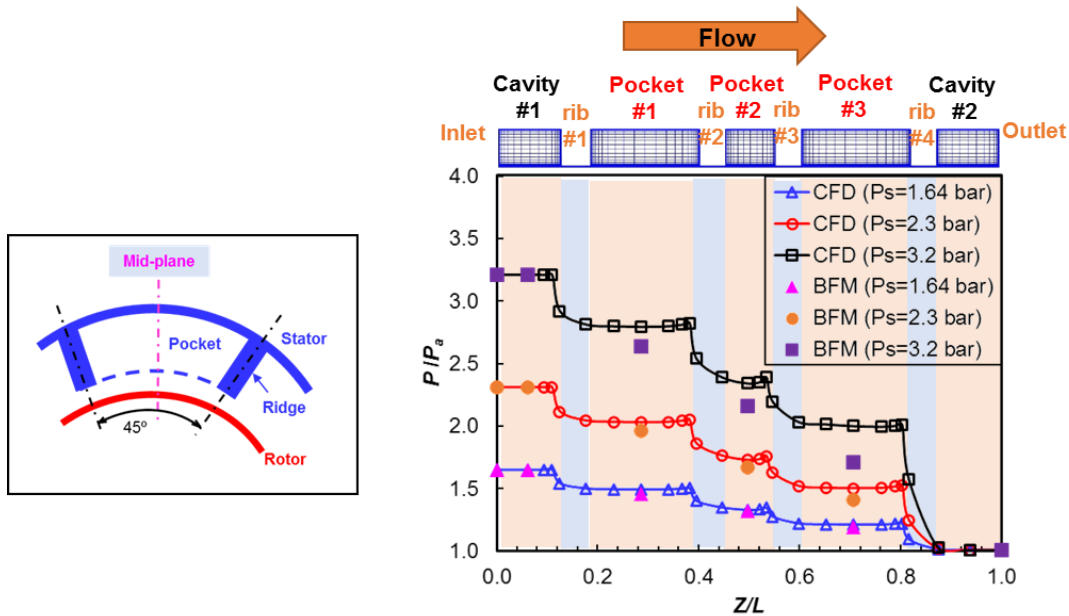
Fig. 12 CFD and BFM predicted average static pressure (*P*) at a mid-plane of a pocket vs. axial direction. Operation at three supply pressures *Ps* = 1.64, 2.3 or 3.2 bar (a). Fully partitioned PDS, *L/D* = 0.38, C_r = 0.184 mm, P_a = 1 bar, rotor speed 5,250 rpm (ΩR = 35 m/s).
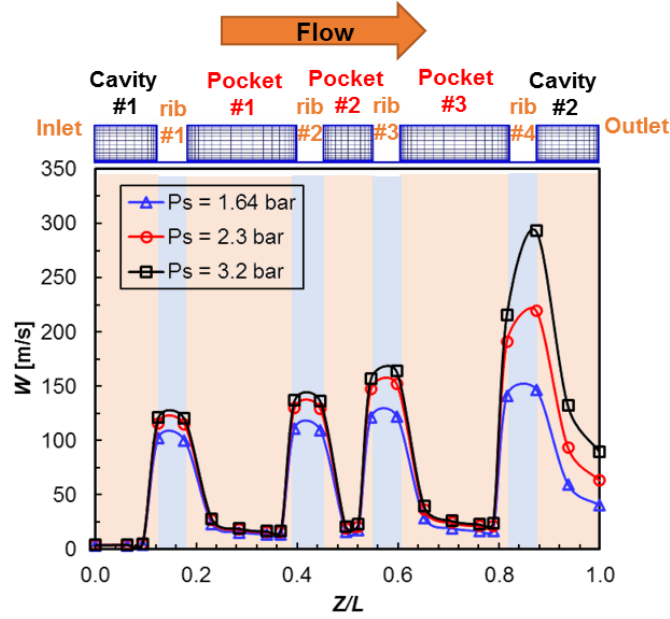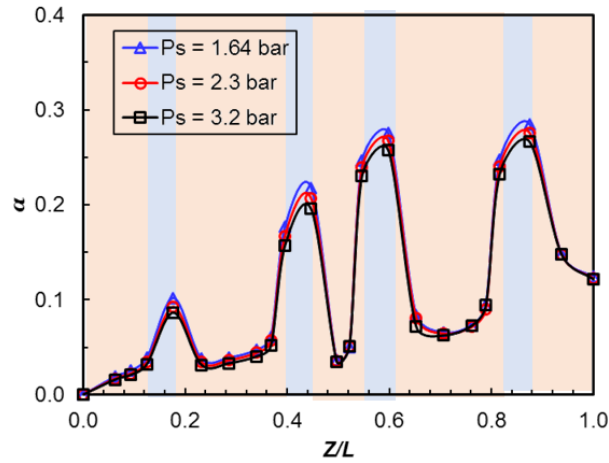
Fig. 13 CFD predicted average axial velocity *W* and swirl ratio *α* at a mid-plane of a pocket vs. axial direction. Operation at three supply pressures *P$_S$* = 1.64, 2.3 or 3.2 bar (a). Fully partitioned PDS, *L/D* = 0.38, *C$_r$* = 0.184 mm, *P$_a$* = 1 bar, rotor speed 5,250 rpm (ΩR = 35 m/s).

Measured and CFD predicted rotordynamic force coefficients

A three-dimensional unsteady state CFD predicts the seal rotordynamic force coefficients. As introduced in an earlier section, a multi-frequency, elliptic orbit method is employed to calculate the seal reaction force variation with time. In the analysis, there are seventeen excitation frequencies, $\{\omega_i\}$ = 10 Hz, 20 Hz, …, 170 Hz (*N* = 17). The time for a complete period of multiple-frequency excitation is *T* = 0.1s. The time step is 0.2 ms (500 steps to complete *T*=0.1 s).

The CFD analysis uses resources from the HPRC in TAMU: 40 cores per one three-dimensional unsteady state flow case. It takes ~25 h CPU time to compute one period of rotor whirl motion. After at least four periods ($4T$) the unsteady state flow simulation converges, as determined from the difference of CFD predicted rotordynamic force coefficients from the third period and fourth period being within 3%.

Figure 14 displays CFD predicted, BFM predicted, and measured direct dynamic stiffness H_R, cross-coupled dynamic stiffness h_R, direct damping C, and effective damping C_{eff} vs. frequency ratio (ω/Ω). Recall the test coefficients are obtained from single frequency dynamic loads. The test data shown is the arithmetic average of the coefficients along the X and Y direction. The vertical error bars in the test data represent the variability of the coefficients along the X and Y directions. Note the measured h_R is very small, thus its variability is relatively high.

Two meshes are used in CFD analysis, one mesh with node count 3.6×10^6, and a finer mesh with node count 5.7×10^6. The predicted H_R and h_R by the mesh with a node count 3.6×10^6 slightly deviates from those from the fine mesh, whereas the predictions of C by using these two meshes agree well. Considering the small difference magnitudes of H_R and h_R, the mesh with 3.6×10^6 node count is good enough for the CFD investigation.

The CFD predicted H_R, increasing with excitation frequency ω, is slightly higher than the test result. The CFD predictions of cross-coupled dynamic stiffness h_R are nearly constant, agreeing with the measured h_R. The direct damping coefficient C predicted by CFD is a little lower than the measured one and decreases slowly with an increase in ω. Thus, the CFD predicted effective damping coefficient is lower than the test data. The measured C_{eff} is positive without a cross-over frequency, whereas the CFD predicted cross-over frequency is ~16 Hz. The predicted cross-coupled damping (c) is very small, c ~0.05 kN-s/m at $\omega = 10$ Hz, thus not shown here. The BFM predictions are lower than the CFD results; so low that the BFM predicted direct damping C is close to zero, hence, the BFM predicted effective damping coefficient is negative.
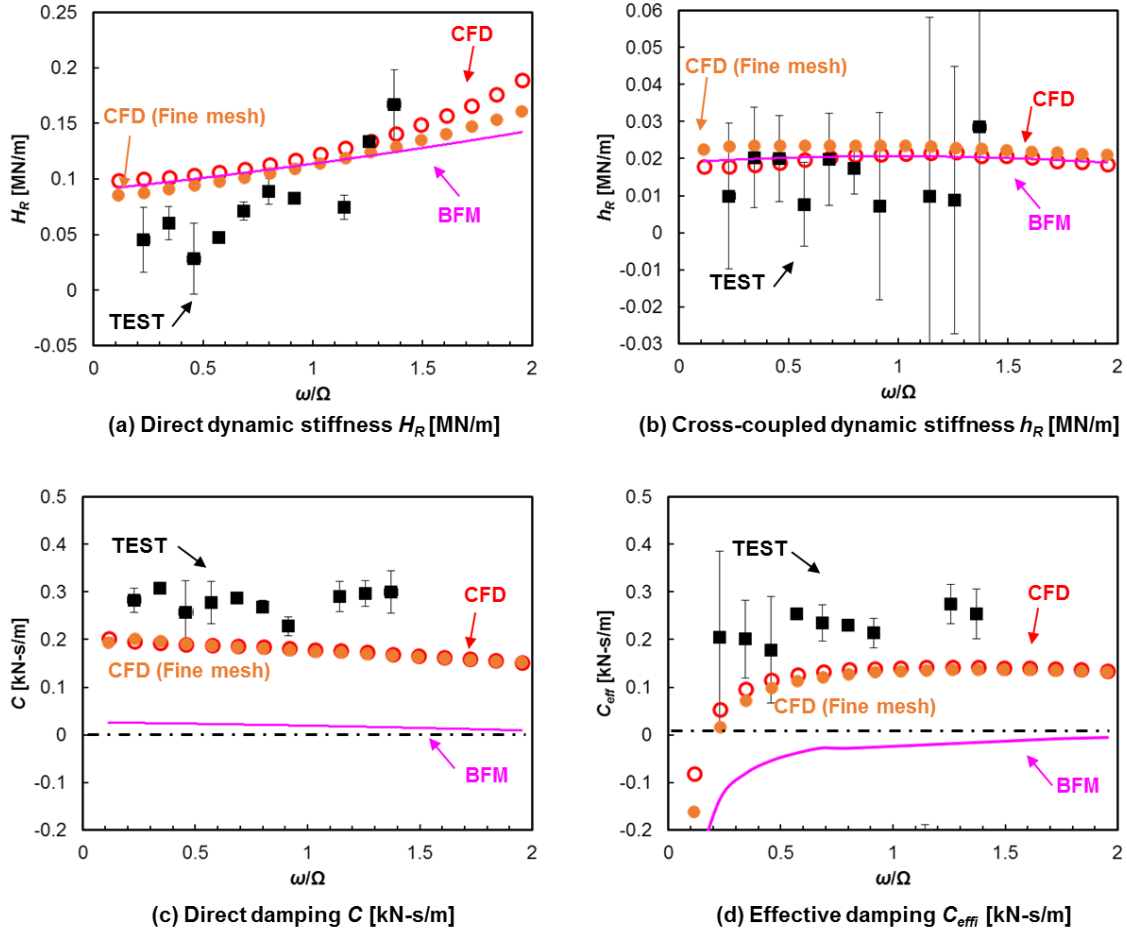
Fig. 14 CFD predicted, BFM[4] predicted and measured rotordynamic force coefficients vs. (ω/Ω). Operation at supply pressure P_s = 2.3 bar. (a) Direct dynamic stiffness H_R, (b) Cross-coupled dynamic stiffness h_R, (c) Direct damping C, (d) Effective damping C_{eff}. Fully partitioned PDS, L/D = 0.38, C_r = 0.184 mm, P_a = 1 bar, rotor speed 5,250 rpm (ΩR = 35 m/s).

In a further numerical test, the CFD and BFM predict the rotordynamic performance for operation under a supply pressure P_s = 3.2 bar (a). Figure 15 displays CFD and BFM predictions of the force coefficients for P_s = 2.3 bar (a) and 3.2 bar (a). H_R increases with an increase in P_s, in particular at a high excitation frequency ($\omega/\Omega > 1$). h_R increases slightly as P_s increases from 2.3 bar to 3.2 bar. The increase of P_s influences most the direct damping C. C almost doubles when (ω/Ω) = 0.1. The cross-over frequency decreases to ~12 Hz for P_s = 3.2 bar (a).

---

[4] The BFM prediction sets all the blades (ribs) active in *PD_Seal®*.
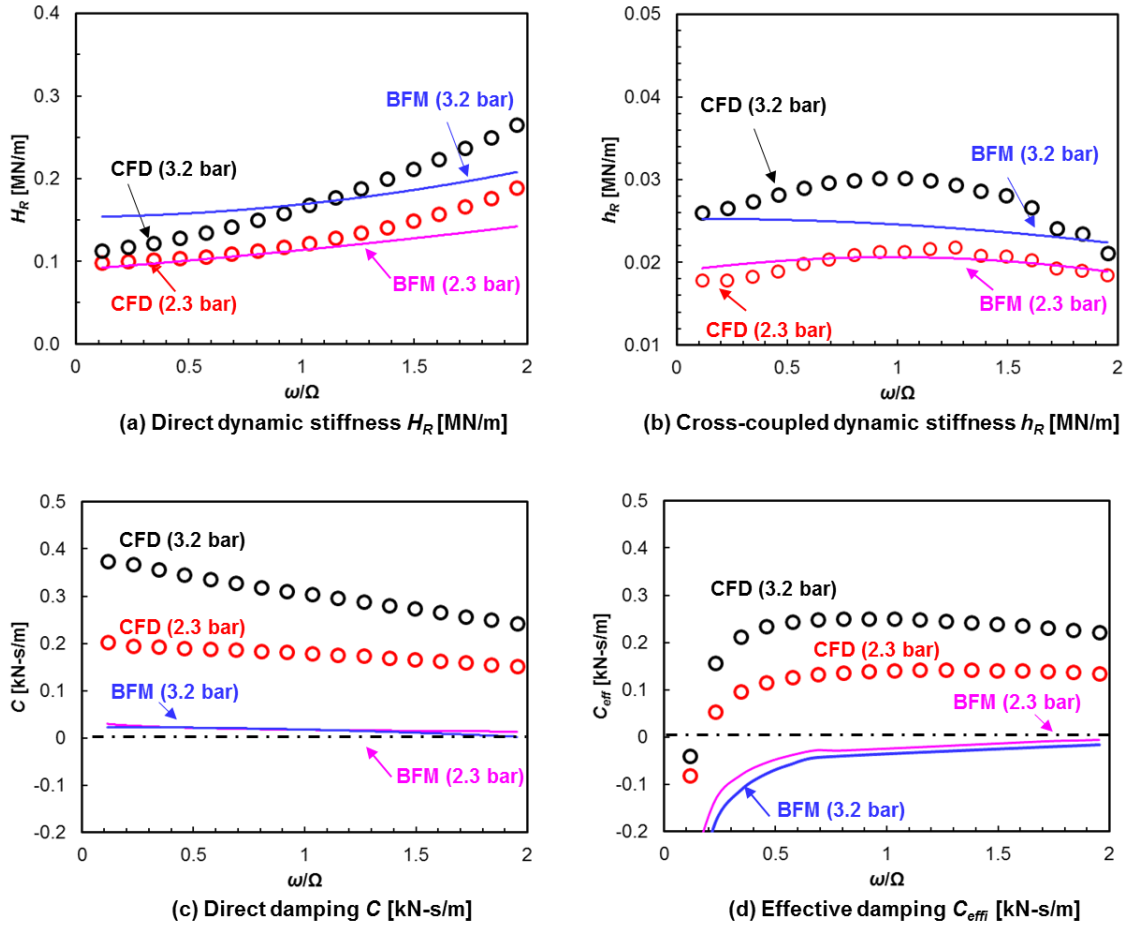
Fig. 15 CFD and BFM predicted rotordynamic force coefficients vs. (ω/Ω). Operation at two supply pressures P_s = 2.3 bar and 3.2 bar. (a) Direct dynamic stiffness H_R, (b) Cross-coupled dynamic stiffness h_R, (c) Direct damping C, (d) Effective damping C_{eff}. Fully partitioned PDS, L/D = 0.38, C_r = 0.184 mm, P_a = 1 bar, rotor speed 5,250 rpm (ΩR = 35 m/s).

4. CFD ANALYSIS OF *WET* GAS FULLY PARTITIONED POCKET DAMPER SEAL

The seal discussed in the last section is used for further tests conducted under a *wet* gas condition. An ISO VG10 oil supplied at temperature T_S = 42°C and mixes with an air stream well upstream of seal inlet, see Refs. [18-19] for details. Table 5 lists the operating condition of the FPPDS. For seal geometry information, refer to Table 3. Note ρ_l/ρ_g = 728 and μ_l/μ_g = 400.

The CFD analysis employs an Eulerian model to predict the two-phase flow. In the model, the gas and liquid components share the static pressure field while having independent velocities. The turbulence flow model is a realizable k-ε model with a scalable wall function. The inlet liquid volume fraction (LVF) is specified at the seal inlet plane. The two-phase flow CFD analysis uses the mesh with node count 3.6×10^6, and displayed in Figure 10.

Table 5 Operating conditions for a *wet* gas FPPDS (See Table 3 for geometry).

Working fluid	Oil in air mixture
Supply pressure, P_S	2.3 bar (a)
Exit pressure, P_e	1 bar (a)
Supply temperature, T_S	315 K
Air density at (P_S, T_S), ρ_g	1.14 kg/m^3
Kinematic viscosity at (P_S, T_S), μ_g	1.8×10^{-5} kg/(m·s)
Oil density, ρ_l	830 kg/m^3
Viscosity at (P_S, T_S), μ_l	8.2 cP
Rotor speed, Ω	5,250 rpm
Surface speed, ΩR	35 m/s
Air sound speed a_g at T_S	356 m/s
Oil sound speed a_l at T_S	1475 m/s
Liquid volume fraction (LVF)	0, 0.4%, 2.2%
Mixture sound speed, a_m	180 m/s for LVF = 0.4% 87 m/s for LVF = 2.2%

Table 6 lists the measured and CFD predicted leakage for the mixture ($\dot{m}$) and the oil only ($\dot{m}_l$) for pressure ratio P_S/P_a = 2.3 and inlet LVF = 0.4%, and for P_S/P_a = 3.2 and inlet LVF = 2.2%. The CFD predicted leakage is ~6% higher than the test data. Note that liquid mass fraction LMF = ($\dot{m}_l/\dot{m}$) is rather large, 57% to 84%, albeit the LVF is just 0.4% and 2.2%. This is due to the large density difference between the two components (ρ_l/ρ_g = 728).

Table 6 Leakage prediction and test data for a *wet* gas FPPFD (*L/D* = 0.38, C_r = 0.184 mm, Rotor speed 5,250 rpm, ΩR = 35 m/s, P_a=1.00 bar, Temperature *T* = 42ºC).

Case No.	Operating conditions			Test data		CFD	
	P_S/P_a	Inlet LVF	Inlet LMF	$\dot{m}$ [g/s]	$\dot{m}_l$ [g/s]	$\dot{m}$ [g/s]	$\dot{m}_l$ [g/s]
1	2.3	0.4%	57%	27.2±3	15.5	28.4	16.1
2	3.2	2.2%	84%	68.7±3	57.5	69.3	58.3

The LVF at the seal outlet plane equals [23]

$$LVF_{out} = \frac{P_a \cdot LVF_{in}}{P_s \cdot (1 - LVF_{in}) + P_a \cdot LVF_{in}} \tag{7}$$

The LVF, Eqn. (7), at the outlet plane is 0.17% for case 1 and 0.7% for case 2, respectively. The CFD predictions equal 0.17% and 0.7%, matching well the analytical result.

Figure 16 displays contours of static pressure (P) on the stator and the rotor surfaces. The static pressure on both rotor and stator surfaces decreases gradually towards $P_a = 1.0$ bar at the seal outlet plane. On the rotor surface, P is slightly lower near the ridges than in the adjacent areas. Figure 17 shows contours of LVF on the stator and rotor surfaces and on the mid-plane (near the seal outlet). The LVF on the rotor surface decreases from 0.4% to 0.17% along the flow direction. The LVF distributions on both surfaces show a similar trend, except at the location near the seal exit cavity (#2). Note at this #2 cavity, as seen in Fig. 17(c), the LVF on the stator surface ~ 0, while on the rotor surface LVF ~0.18%. The results thus show the bulk of the oil attaches near the rotor surface whereas air, nearly stagnant, fills in most of the exit cavity (LVF~0) after leaving the last (#4) rib.

Figure 18 displays the average static pressure (P) and average LVF along the axial direction (Z/L) at a mid-plane of a pocket. P decreases when the fluid leaves a pocket and enters a film below a rib. The LVF decreases when the fluid mixture passes below a rib and enters a pocket.

Figure 19 displays the average axial velocity W and swirl ratio α vs. axial length (Z/L). Within the PDS, the mixture accelerates when the axial area converges, i.e. when the fluid flows through the clearance below a rib. The average W_l and W_g along the axial direction are identical. Similarly, the average α_l and α_g along the axial direction equal each other. The air circumferential velocity increases as the fluid passes below a rib. Both α_l and α_g are less than 0.2 within the seal. Hence, the oil in air flow is homogeneous

After the mixture leaves the final rib (#4), the flow area suddenly increases in the exit cavity (#2). As shown in Fig. 19, the air cross-film average velocities, both axial and circumferential, decrease due to the cross-section area expansion. On the other hand, the oil decelerates to give a lesser cross-film average velocity. However, as the insets show, both the oil and air remain attached to the rotor surface within a layer just a few times thicker than the clearance. Similarly, the circumferential velocity or swirl (α) remains the same for both components. Thus, as the flow within the PDS, the flow remains homogenous within this layer attached to the rotor.

(a) Static pressure on stator surface [bar]

(b) Static pressure on rotor surface [bar]
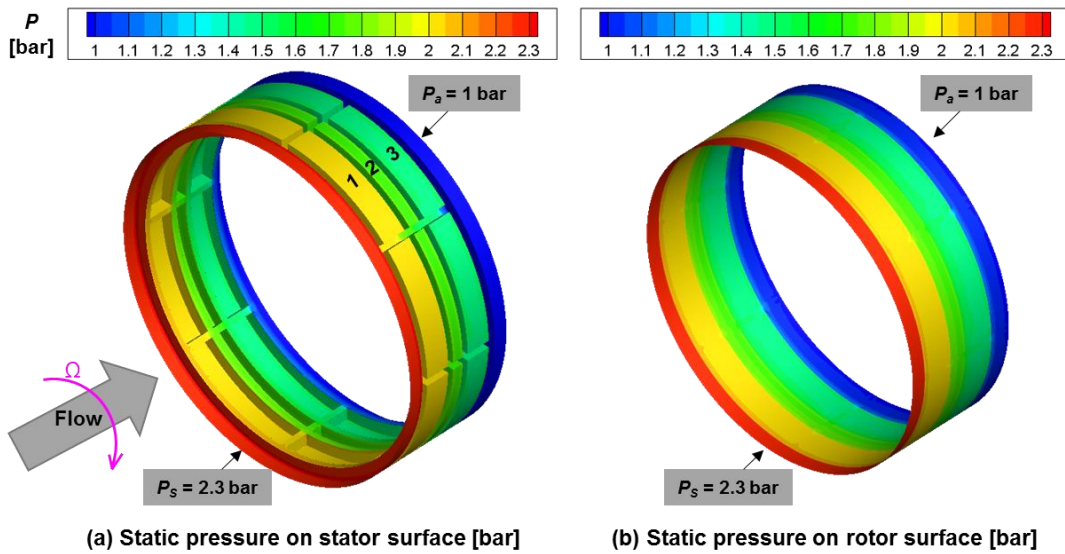
Fig. 16 CFD predicted static pressure P on stator and rotor surfaces. Operation at P_s = 2.3 bar (a) and inlet LVF = 0.4%. Fully partitioned PDS, L/D = 0.38, C_r = 0.184 mm, rotor speed 5,250 rpm (ΩR = 35 m/s).

(a) LVF on stator surface

(b) LVF on rotor surface

(c) LVF near the seal outlet on the mid-plane

Fig. 17 CFD predicted LVF contour on stator and rotor surfaces and on the mid-plane. Operation at P_s = 2.3 bar (a) and inlet LVF = 0.4%. Fully partitioned PDS, L/D = 0.38, C_r = 0.184 mm, rotor speed 5,250 rpm (ΩR = 35 m/s).

30
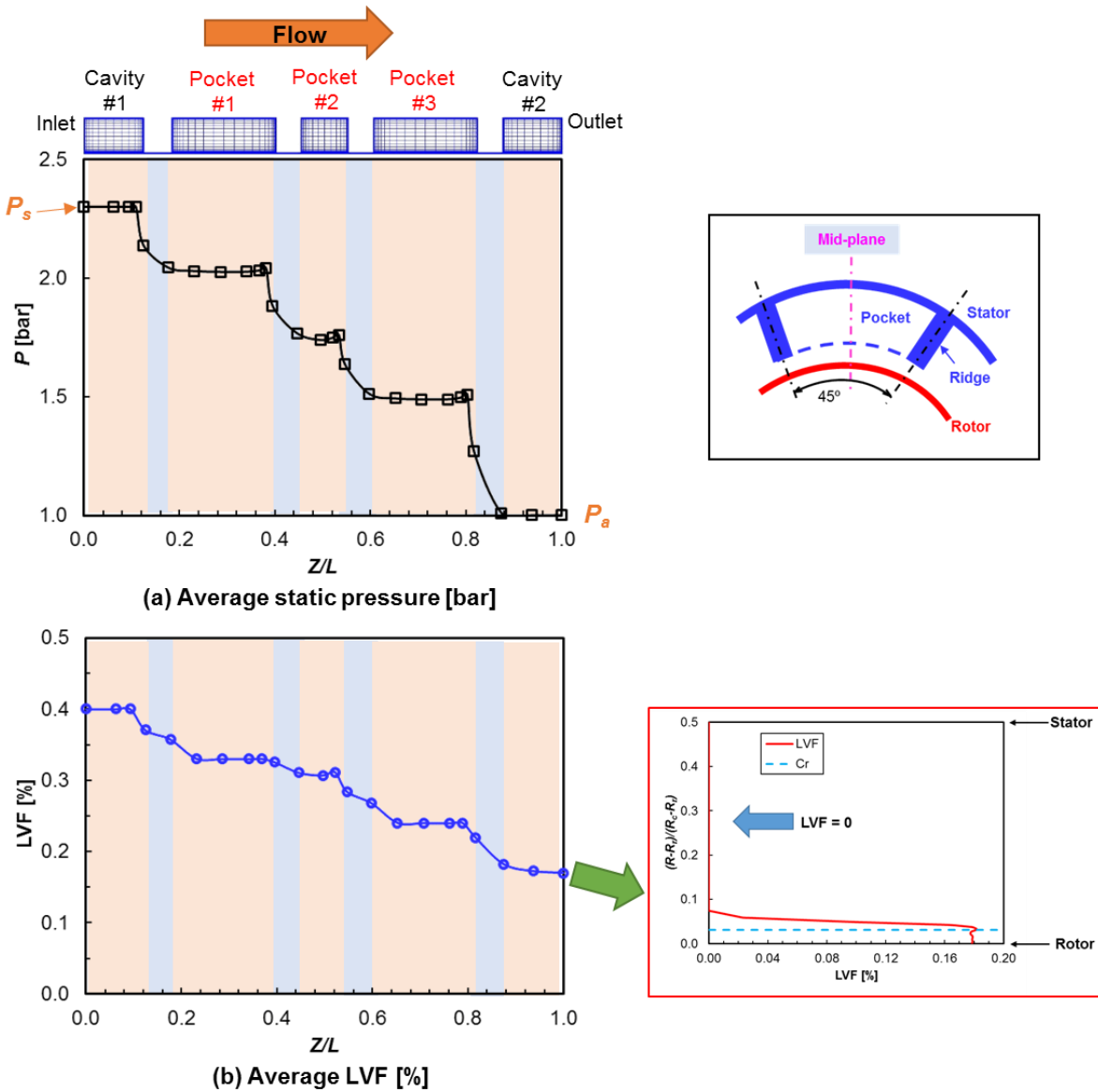
Fig. 18 CFD predicted cross-film average static pressure *P* and LVF vs. axial direction at the mid-plane of a pocket. Inset on the right shows LVF at the seal exit cavity plane. Operation at P_s = 2.3 bar (a) and inlet LVF = 0.4%. Fully partitioned PDS, *L/D* = 0.38, C_r = 0.184 mm, rotor speed 5,250 rpm (ΩR = 35 m/s).

31
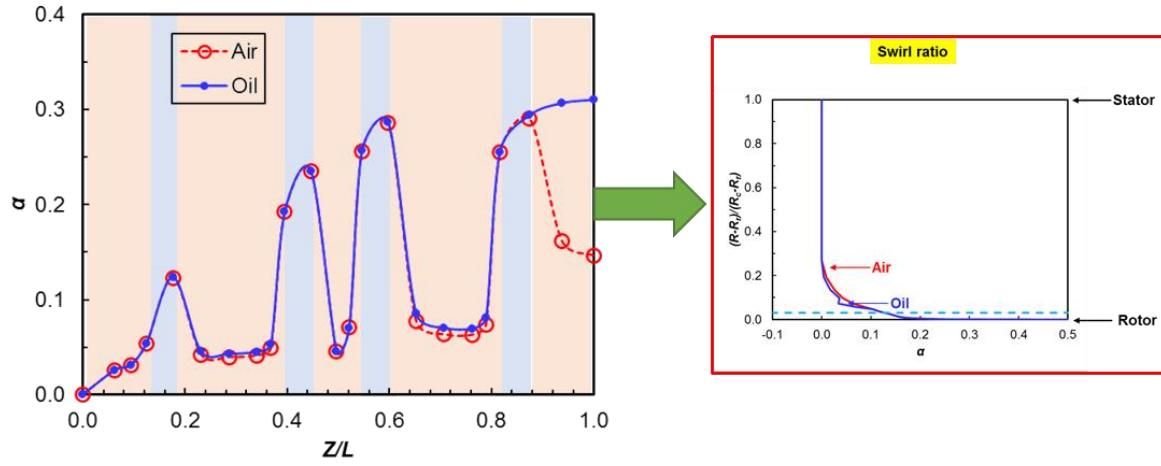
Fig. 19 CFD predicted cross-film average axial velocity *W* and swirl ratio *α* vs. axial direction at a mid-plane of a pocket. Insets show velocity profiles at the seal exit cavity plane. Operation at P_s = 2.3 bar (a) and inlet LVF = 0.4%. Fully partitioned PDS, L/D = 0.38, C_r = 0.184 mm, rotor speed 5,250 rpm (ΩR = 35 m/s).
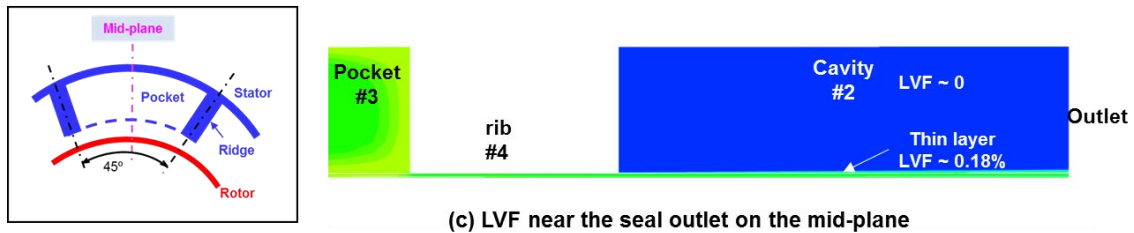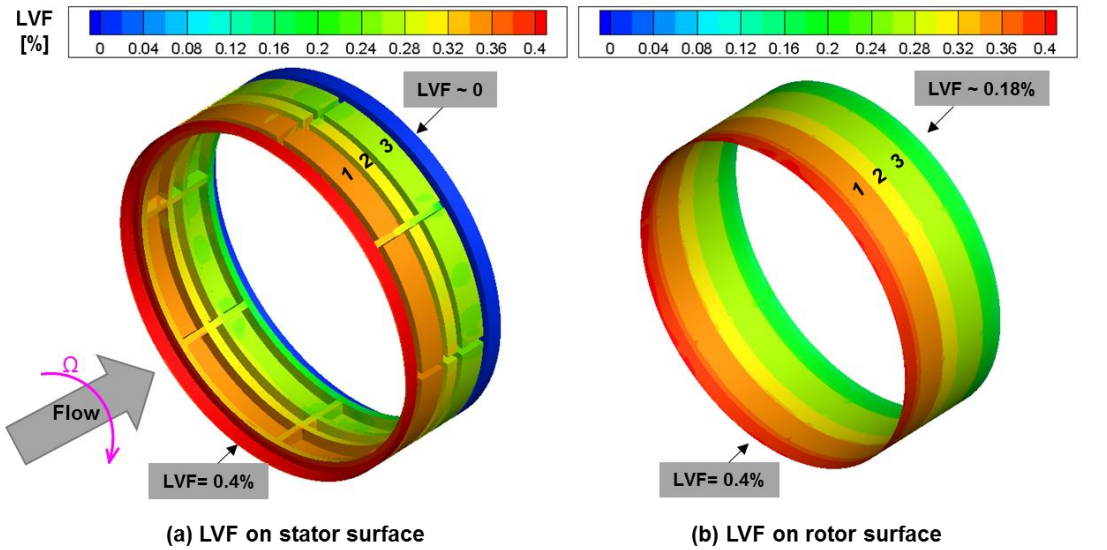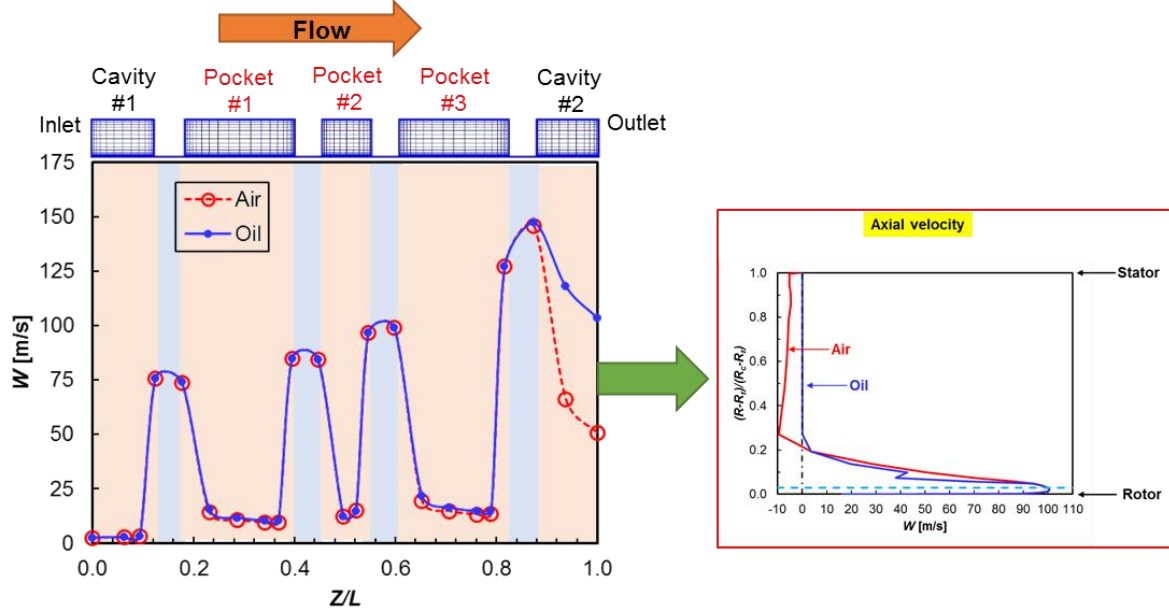
Recall the axial flow Reynolds number (Re_a) and circumferential flow Reynolds number (Re_c) equal

$$\text{Re}_a = \frac{\rho_m W_m C_r}{\mu_m} = \frac{\dot{m}}{\pi D \mu_m}, \quad \text{Re}_c = \frac{\rho_m (\Omega R) C_r}{2\mu_m}, \quad \text{Re} = \sqrt{\text{Re}_a^2 + \text{Re}_c^2} \tag{8}$$

where W_m is the axial velocity of the mixture, ρ_m is the mixture density, $\rho_m = \text{LVF} \cdot \rho_l + (1-\text{LVF}) \cdot \rho_g$, and μ_m is the mixture viscosity, $\mu_m = \text{LVF} \cdot \mu_l + (1-\text{LVF}) \cdot \mu_g$. Based on Figure 19(a), $W_m = W_l = W_g$.

Table 7 lists the Reynolds number for the FPPDS operating with *wet* gas (inlet LVF = 0.4%) and operating with just air under same supply pressure P_S = 2.3 bar. Compared with operation with just air, both Re_a and Re_c decrease for the *wet* gas condition. Importantly enough, akin to a *Rossby* #, the ratio (Re_a/Re_c) is much greater than one thus denoting the dominance of the extrusion (axial) flow over the circumferential flow. This explains why the mixture remains attached to the rotor as it exits the PDS.

Table 7 Axial and circumferential[5] Reynolds numbers for a FPPDS, dry and *wet* gas (inlet LVF = 0.4%) condition. Operation at P_S = 2.3 bar. (*L/D* = 0.38, C_r = 0.184 mm, Rotor speed 5,250 rpm, ΩR = 35 m/s, P_a=1.00 bar, Temperature *T* = 42ºC).

|	Re_a	Re_c	Re	Re_a/Re_c
Dry gas	2,560	193	2,568	13
Wet gas	1,319	277	1,348	5

(LVF = 0.4%, ρ_m = 4.5 kg/m³, μ_m = 5.1×10⁻⁵ kg/(m·s), a_m = 180m/s)

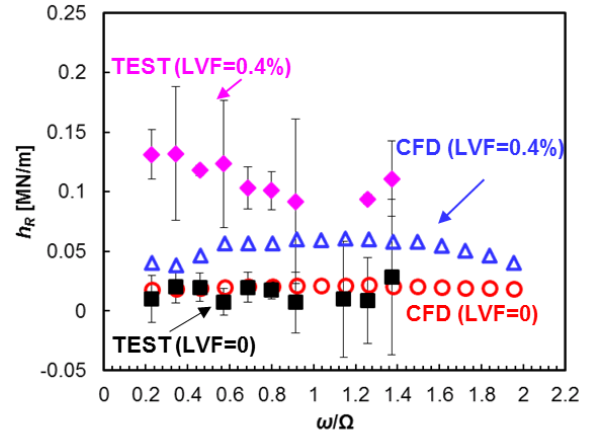**Measured and CFD predicted rotordynamic coefficients for *wet* gas FPPDS**

Figure 20 shows the experimental identified and CFD predicted rotordynamic force coefficients for operation with supply pressure P_s = 2.3 bar and inlet LVF = 0 (pure air) and 0.4%. For the test data, a small volume of oil (LVF = 0.4%) added into the air stream produces a significant influence on the seal force coefficients. The measured direct dynamic stiffness H_R turns negative under a *wet* gas condition; alas the CFD predicted H_R remains positive and increases slightly when compared with the prediction for pure air. The measured cross-coupled dynamic stiffness h_R and direct damping C both increase significantly in comparison with the test data for the pure air condition. The CFD predicted h_R and C are slightly higher than those for the seal operating with pure gas (inlet LVF = 0), respectively. In the CFD prediction, the effective damping C_{eff} for the PDS operating with a *wet* gas is lower than that for the seal with air only. The cross-over frequency for the *wet* gas FPPDS is ~ 22Hz.

The difference between the CFD predicted and the test coefficients under a *wet* gas condition, in particular H_R, is inexplicable. Note the test data also show a high variability between *X* and *Y* directions. Both experimental and CFD results show the flow in the *wet* gas FPPDS is complex.
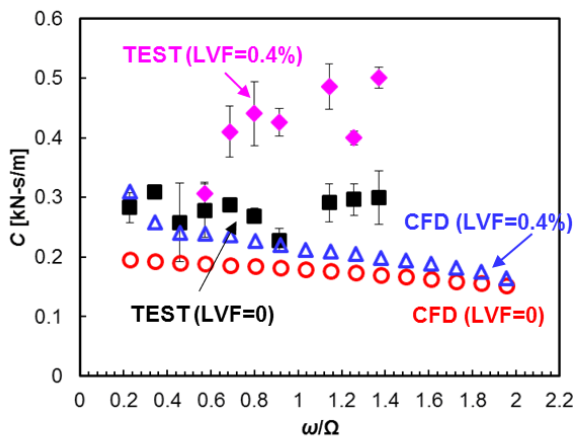
---

[5] Indeed, the circumferential flow is very small compared to the axial flow. Hence, the liquid is pushed forward (and attached to the closest wall: rotor) as it is also shear driven by rotation. On the other hand, the air merely expands.
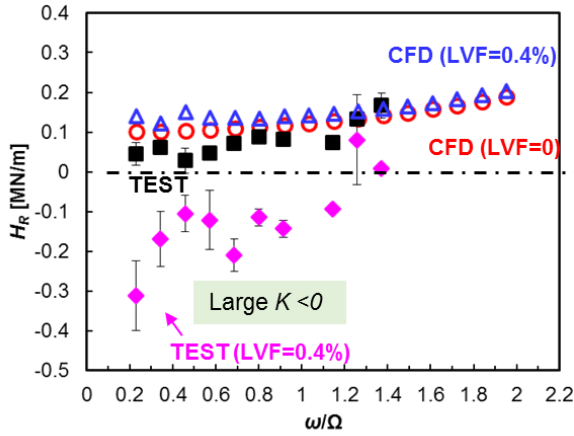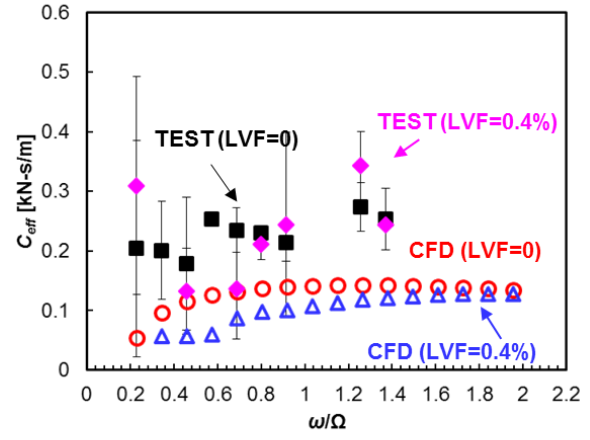
Fig. 20 CFD predicted and measured rotordynamic force coefficients for *wet* gas FPPDS vs. frequency ratio (ω/Ω). Operation at P_s = 2.3 bar (a) and inlet LVF = 0.4%. (a) Direct dynamic stiffness H_R, (b) Cross-coupled dynamic stiffness h_R, (c) Direct damping C, (d) Effective damping C_{eff}. Fully partitioned PDS, L/D = 0.38, C_r = 0.184 mm, rotor speed 5,250 rpm (ΩR = 35 m/s).

5. CONCLUSION

In a liquid tolerant compression system [16-17], a pocket damper seal (PDS) has shown a superior stability characteristics under *wet* gas operation other than a labyrinth seal of the same dimensions. The circumferential ridges in a PDS can limit or remove the trapped liquid swirling in the cavities. Thus, PDSs have a promising application in multi-phase pump and compression systems in subsea facilities. To date there is scant literature, experimental or numerical, addressing to the performance of *wet* gas PDSs. Therefore, the report details a comprehensive investigation, both experimental and numerical, and discusses the performance of a PDS operating with a gas and moving towards *wet* gas.

The CFD model, implementing a multi-frequency, elliptic orbit method and Discrete Fourier Transform (DFT), procures the rotordynamic force coefficients for an eight-ribs FPPDS operating with an air supply pressure P_S = 6.9 bar and rotor speed 15,000 rpm (ΩR = 134 m/s). The CFD predictions are validated against test data in Ref. [7]. Besides CFD, a bulk-flow model ($PD\_Seal^{\circledR}$) is also used for benchmarking. The CFD predicted direct dynamic stiffness H_R and cross-coupled dynamic stiffness h_R match well the test data. The CFD predicted direct damping C is smaller than the test result. The BFM under estimates H_R and over predicts h_R. Though the BFM predictions deviate from the test data, the simple model still captures the variation trends of the seal force coefficients.

The report includes both experimental results and CFD predictions for a four-ribs FPPDS (L/D = 0.38, C_r = 0.184 mm), built and tested at the Turbomachinery Laboratory. Both the CFD and BFM predicted leakage agree with the test data for the FPPDS operating under pressure ratio P_S/P_a = 2.3, rotor speed 5,250 rpm (ΩR = 35 m/s) and inlet LVF = 0 (pure air). The CFD predicted direct dynamic stiffness (H_R) increases with excitation frequency ratio (ω/Ω). While the direct damping (C) is slightly lower than the test data. When the FPPDS operates with a *wet* gas (ISO VG10 oil in air mixture, inlet LVF = 0.4%), the measured force coefficients show great variability. H_R becomes negative, whereas the CFD prediction is opposite, $H_R > 0$. For the seal operating with a *wet* gas, the test cross-coupled dynamic stiffness (h_R) and direct damping (C) both increase, as compared to the coefficients for the gas only seal. In comparison with the predicted coefficients for gas only condition, CFD predictions of h_R and C vs. frequency under *wet* gas condition both increase as the test data does, while with smaller change magnitudes. The CFD accurately predicts the leakage for the FPPDS operating with gas only or with a *wet* gas. The gap between the CFD predicted and experimental derived force coefficients for *wet* gas FPPDS shows the complexity of the two-phase flow in a FPPDS. Further work will continue to push the technology of *wet* gas seals while bridging the gap between test data and computational physics model simulations.

NOMENCLATURE

a	Sound speed [m/s]
C_r	Seal radial clearance [m]
C	Direct damping coefficients [Ns/m]
C_{eff}	Effective damping coefficient [Ns/m], $C_{eff} = C - h_R/\omega$
d	Pocket depth [m]
d_x, d_y	Rotor displacement components (radial and tangential) [m]
D_r	$2R_r$. Rotor diameter [m]
D_s	$2R_s$. Stator diameter [m]
f_x, f_y	Seal reaction force components (radial and tangential) [N]
F_X, F_Y	Seal reaction force components in frequency domain [N]
H_R, h_R	Direct and cross-coupled dynamic stiffnesses [N/m]
H_I, h_I	Direct and cross-coupled quadrature stiffnesses [N/m]
$\bar{H}, \bar{h}$	Direct and cross-coupled impedances [N/m]
K, k	Direct and cross-coupled stiffnesses [N/m]
L	Seal land length [m]
L_C	Pocket length [m]
$\dot{m}$	Leakage (mass flow rate) [kg/s]
Ma	Mach number, $Ma = W/a$
P	Static pressure [Pa]
P_S, P_a	Supply and discharge pressures [Pa]
Re_a, Re_c	Axial and circumferential Reynolds number, $Re_a = (\rho W C_r)/\mu$, $Re_c = (\rho \Omega R C_r)/(2\mu)$
R_r	Rotor radius [m]
R_s	Stator radius [m]
T	Period of rotor whirl [s]
T_S	Temperature of supply fluid [K]
U_θ, W	Average (cross-film) circumferential and axial flow velocities [m/s]
X, Y, Z	Inertial coordinate system
α	Circumferential swirl ratio, $\alpha = U_\theta/(\Omega R)$
δ	Rib axial thickness [m]
ΔP	Pressure drop [Pa], $\Delta P = P_s - P_a$
θ	Circumferential coordinate [rad]
μ	Viscosity [Pa·s]
v	Kinematic viscosity [m²/s]
ρ	Density, [kg/m³]
ω	Whirl frequency [rad/s]
Ω	Rotor angular velocity [rad/s]

Abbreviations

BFM	Bulk-flow model
CFD	Computational Fluid Dynamics
DFT	Discrete Fourier Transform
FPPDS	Fully Partitioned Pocket Damper Seal
GVF	Gas volume fraction
HCS	Honeycomb seal
LABY	Labyrinth Seal
LVF	Liquid volume fraction

LMF   Liquid mass fraction
PDS   Pocket Damper Seal
SSV   Sub synchronous vibration

Subscripts

g   Gas
l   Liquid
m   Mixture
in   Seal inlet plane
out   Seal outlet plane
R   Real part of a complex number
I   Imaginary part of a complex number

REFERENCES

[1] Vance, J. M., and Shultz, R. R, 1993, "A New Damper Seal for Turbomachinery," Proc. of the 14th Vibration and Noise Conference, September 19-22, Albuquerque, NM, ASME DE-60, pp. 139-148.

[2] Vance, J. M., and Li, J., 1996, "Test Results of a New Damper Seal for Vibration Reduction in Turbomachinery," ASME J. Eng. Gas Turbines Power, **118**(10), pp. 843-846.

[3] Ransom, D., Li, J., San Andres, L., and Vance, J. M, 1999, "Experimental Force Coefficients for a Two-Bladed Labyrinth Seal and a Four-Pocket Damper Seal," ASME J. Tribol., **121**(4), pp. 370-376.

[4] Ertas, B. H., Delgado, A., and Vannini, G., 2006, "Rotordynamic Force Coefficients of Pocket Damper Seals," ASME J. Turbomach., **128**(10), pp. 725-737.

[5] Li, J., Kushner, F., and DeChoudhury, P., 2002, "Experimental Evaluation of Slotted Pocket Damper Seals on a Rotating Test Rig," ASME GT-2002-30634.

[6] Ertas, B. H., and Vance, J. M., 2007, "Rotordynamic Force Coefficients for a New Damper Seal Design," ASME J. Tribol., **129**(4), pp. 365-374.

[7] Ertas, B. H., Delgado, A., and Vannini, G., 2012, "Rotordynamic Force Coefficients for Three Types of Annular Gas Seals with Inlet Pre-swirl and High Differential Pressure Ratio," ASME J. Eng. Gas Turbines Power, **134**(4), p. 042503.

[8] Li, J., San Andrés, L., and Vance, J. M, 1999, "A Bulk-Flow Analysis of Multiple-Pocket Gas Damper Seals," ASME J. Eng. Gas Turbines Power, **121**(4), pp. 355-363.

[9] Li, J., Ransom, D., San Andrés, L., and Vance, J. M, 1999, "Comparison of Predictions with Test Results for Rotordynamic Coefficients of a Four-Pocket Gas Damper Seal," ASME J. Tribol., **121**(4), pp. 363-369.

[10] Li, J., Aguilar, R., San Andrés, L., Vance, J. M, 2000, "Dynamic Force Coefficients of a Multiple-Blade, Multiple-Pocket Gas Damper Seal: Test Results and Predictions," ASME J. Tribol., **122**(1), pp. 317-322.

[11] Li, J., Li, Z., and Feng, Z., 2012, "Investigations on the Rotordynamic Coefficients of Pocket Damper Seals Using the Multi-frequency, One-Dimensional, Whirling Orbit Model and RANS Solutions," ASME J. Eng. Gas Turbines Power, **134**(10), pp. 102510.

[12] Li, Z., Li, J., and Yan, X., 2013, "Multiple Frequency Elliptical Whirling Orbit Model and Transient RANS Solution Approach to Rotordynamic Coefficients of Annular Gas Seals Prediction," ASME J. Vib. Acoust., **135**(7), pp. 031005.

[13] Li, Z., Li, J., and Feng, Z., 2015, "Numerical Investigations on the Leakage and Rotordynamic Characteristics of Pocket Damper Seals Part I: Effects of Pressure Ratio, Rotational Speed, and Inlet Pre-swirl," ASME J. Eng. Gas Turbines Power, **137**(3), p. 032503.

[14] Li, Z., Li, J., and Feng, Z., 2015, "Numerical Investigations on the Leakage and Rotordynamic Characteristics of Pocket Damper Seals Part II: Effects of Partition Wall Type, Partition Wall Number, and Cavity Depth," ASME J. Eng. Gas Turbines Power, **137**(3), p. 032504.

[15] Li, Z., Li, J, and Feng, Z., 2016, "Numerical Comparison of Rotordynamic Characteristics for a Fully Partitioned Pocket Damper Seal and a Labyrinth Seal with High Positive and Negative Inlet Pre-swirl," ASME J. Eng. Gas Turbines Power, **138**(4), p. 042505.

[16] Vannini, G, Bertoneri, M., Del Vescovo, G., Wilcox, M., 2014, "Centrifugal Compressor Rotordynamics in Wet Gas Conditions," Proc. 43rd Turbomachinery Symposium, September 22-25, Houston, TX, pp. 201-220.

[17] Vannini, G., Bertoneri, M., Nielsen, K. K, Ludiciani, P., and Stronach, R., 2016, "Experimental Results and Computational Fluid Dynamics Simulations of Labyrinth and Pocket Damper Seals for Wet Gas Compression," ASME J. Eng. Gas Turbines Power, **138**(5), pp. 052501.

[18] San Andrés, L., Lu, X., and Liu, Q., 2016, "Measurements of Flow Rate and Force Coefficients in a Short-Length Annular Seal Supplied with a Liquid/Gas Mixture (Stationary Journal)," Tribol. Trans., **59** (4), pp. 758-767.

[19] San Andrés, L., and Lu, X., 2018, "Leakage, Drag Power and Rotordynamic Force Coefficients of an Air in Oil (Wet) Annular Seal," ASME J. Eng. Gas Turbine Power, **140**(1), pp. 012505.

[20] Lu, X., and San Andrés, L., 2018, "Leakage and Rotordynamic Force Coefficients of a Three-Wave (Air in Oil) Wet Annular Sea: Measurements and Predictions," ASME Paper No. GT2018-75200.

[21] San Andrés, L., and Lu, X., 2018, "On the Leakage and Rotordynamic Coefficient of Pump Annular Seals Operating with Air/Oil Mixtures: Measurements and Predictions," Proc. of the Asia Turbomachinery & Pump Symposium, Singapore, March 12-15.

[22] Vannini, G., Bertoneri, M., Del Vescovo, G. and Wilcox, M., 2014, "Centrifugal Compressor Rotordynamics in Wet Gas Conditions," Proc. of the 43th Turbomachinery & 30th Pump Users Symposia, Houston, TX, September 23-25.

[23] San Andrés, L., 2012, "Rotordynamic Force Coefficients of Bubbly Mixture Annular Pressure Seals," ASME J. Eng. Gas Turbine Power, **134**(2), pp. 022503.